

INJECTION OF MAGNETIC ENERGY AND MAGNETIC HELICITY INTO THE SOLAR ATMOSPHERE BY AN EMERGING MAGNETIC FLUX TUBE

T. MAGARA AND D. W. LONGCOPE

Department of Physics, Montana State University, Bozeman, MT 59717-3840; magara@solar.physics.montana.edu

Received 2002 August 26; accepted 2002 November 26

ABSTRACT

We present a detailed investigation of the dynamical behavior of emerging magnetic flux using three-dimensional MHD numerical simulation. A magnetic flux tube with a left-handed twist, initially placed below the photosphere, emerges into the solar atmosphere. This leads to a dynamical expansion of emerging field lines as well as an injection of magnetic energy and magnetic helicity into the atmosphere. The field-aligned distributions of forces and plasma flows show that emerging field lines can be classified as either expanding field lines or undulating field lines. A key parameter determining the type of emerging field line is the aspect ratio of its shape (the ratio of height to footpoint distance). The emergence generates not only vertical but also horizontal flows in the photosphere, both of which contribute to injecting magnetic energy and magnetic helicity. The contributions of vertical flows are dominant at the early phase of flux emergence, while horizontal flows become a dominant contributor later. The emergence starts with a simple dipole structure formed in the photosphere, which is subsequently deformed and fragmented, leading to a quadrupolar magnetic structure.

Subject headings: methods: numerical — MHD — Sun: atmosphere — Sun: magnetic fields

1. INTRODUCTION

Magnetic flux emergence has been one of the most important subjects in solar physics because it provides seeds of energetic activity on the Sun. According to prevailing ideas, the magnetic field is initially amplified near the bottom of the convection zone and then starts to rise toward the surface by magnetic buoyancy, finally emerging into the atmosphere. During its residence in the convection zone the magnetic field is believed to form a thin flux tube whose motions are strongly controlled by surrounding convective plasma. A particularly fruitful version of the confined state is the thin flux tube model, which assumes that the magnetic field behaves like a “one-dimensional string” (Spruit 1981; Stix 1991, p. 270). The validity of this model is suggested from observational results for sunspots, whose behavior is related to the evolution of subsurface magnetic fields. Recent work based on this model has successfully explained many observed properties of sunspots, such as latitude, tilt angle, and east-west asymmetry (Choudhuri & Gilman 1987; Howard 1991; D’Silva & Choudhuri 1993; Fan, Fisher, & McClymont 1994; Fisher, Fan, & Howard 1995).

The success of thin flux tube modeling enables us to infer that the invisible subsurface magnetic field is probably composed of slender tubes of twisted flux. The necessity of twist was demonstrated by separate studies in which untwisted tubes could not maintain their integrity in the face of the forces of interaction with the surrounding medium (Schüssler 1979; Longcope, Fisher, & Arendt 1996; Emonet & Moreno-Insertis 1998; Abbett, Fisher, & Fan 2000; Dorch & Nordlund 2001; Dorch et al. 2001).

Although the thin flux tube model has contributed significantly to our understanding of the dynamics of interior magnetic field, it provides less information about the details of flux emergence, where the magnetic field cannot be approximated as a one-dimensional string. The emergence process is essentially dynamical and difficult to study owing to the dramatically changing plasma environment in the

vicinity of the photosphere. The gas pressure drops by 10^{-6} in a few megameters, since the pressure scale height in the photosphere is about 150 km. As this pressure drops abruptly, the magnetic field becomes free to expand into the atmosphere.

A feasible approach to the study of flux emergence is to reproduce the temporal development of emerging magnetic fields by directly solving time-dependent, nonlinear MHD equations. Toward this end, a lot of effort has been devoted to performing MHD numerical simulations in which the confined magnetic field rises from the dense subphotosphere into the tenuous atmosphere. Those numerical simulations were first available for two-dimensional studies, which clarified several important physical processes related to flux emergence, such as the nonlinear Parker instability (Shibata et al. 1989; Shibata, Tajima, & Matsumoto 1990; Tajima & Shibata 1997, p. 189) and the development of the Rayleigh-Taylor instability at the flattening part of an emerging flux tube (Magara 2001).

Recently, three-dimensional flux emergence simulations have been performed that naturally display more realistic and complicated behavior. Most importantly, only three-dimensional simulations permit a flux tube to drain material, thereby reducing the mass carried into the atmosphere. The emerged magnetic field lines form a sigmoidal structure (Matsumoto et al. 1998; Magara & Longcope 2001) and an arch filament system (Fan 2001).

The present work provides further insights into the three-dimensional evolution of flux emergence by studying the field-aligned distributions of forces and flows in individual field lines. This approach clarifies the underlying physics of flux emergence and explains an apparent contradiction in the results reported from the small number of simulations performed to date. In the simulation of Fan (2001) the axis of the tube remains near the photosphere after emergence. In a similar simulation, but using a slightly different profile of flux, Magara & Longcope (2001) observed the axis reaching substantial heights. Our analysis will focus on the

evolution of the axis field line, finding that it is closely related to its geometry. The evolution of the axis field line has been shown to be important in the formation of prominences within sheared coronal field distributed over the neutral line (DeVore & Antiochos 2000).

Our analysis will also quantify the fluxes of magnetic energy and magnetic helicity into the atmosphere during emergence. Some of the previous analyses of this process have used an impenetrable lower boundary and quantified the energy and helicity flux due to horizontal motions alone. Recent observations (Kusano et al. 2002) have shown, however, that the advection of energy and helicity by vertical flows may actually be the dominant effect. Our simulation corroborates this observational finding, showing the advection to be dominant during early phases of emergence.

In the next section we describe the basic equations and the model used in this study. The simulation results are presented in § 3, while § 4 is devoted to a discussion of how the behavior of emerging field lines in the simulation is related to dynamical events observed on the Sun. The final section presents a summary of this study and its applicability to observed solar phenomena.

2. DESCRIPTION OF THE SIMULATION

2.1. Basic Equations

We solve the time-dependent nonlinear, compressible, ideal MHD equations in Cartesian coordinates, with z directed vertically upward. The simulation box is $(-100, -100, -10) \leq (x, y, z) \leq (100, 100, 100)$, in rescaled variables described below. The grid is a Cartesian product of three nonuniform grids, to enhance resolution in critical locations. The finest resolution $\Delta x = \Delta y = \Delta z = 0.2$ occurs within the region $(-8, -8, -10) \leq (x, y, z) \leq (8, 8, 10)$. The grid spacing increases continuously to $\Delta x = \Delta y = \Delta z = 4$ away from this region. The total number of cells in each grid is $N_x \times N_y \times N_z = 215 \times 215 \times 168$.

We advance mass density, velocity, magnetic field, and pressure, denoted ρ , \mathbf{v} , \mathbf{B} , and P , according to the equations of continuity, momentum balance, induction, and the adiabatic gas law,

$$\frac{\partial \rho}{\partial t} + \nabla \cdot (\rho \mathbf{v}) = 0, \quad (1)$$

$$\rho \left[\frac{\partial \mathbf{v}}{\partial t} + (\mathbf{v} \cdot \nabla) \mathbf{v} \right] = -\nabla P + \frac{1}{4\pi} (\nabla \times \mathbf{B}) \times \mathbf{B} + \rho \mathbf{g}, \quad (2)$$

$$\frac{\partial \mathbf{B}}{\partial t} = \nabla \times (\mathbf{v} \times \mathbf{B}), \quad (3)$$

$$\frac{\partial}{\partial t} \left(\frac{P}{\rho^\gamma} \right) + \mathbf{v} \cdot \nabla \left(\frac{P}{\rho^\gamma} \right) = 0. \quad (4)$$

The constants $\mathbf{g} = -g\hat{z}$ and $\gamma = 5/3$ are the gravitational acceleration (downward) and the adiabatic index. Temperature, while not part of the basic equations, may be derived from the ideal gas law

$$P = \frac{\rho \Re T}{\mu} \quad (5)$$

with constant mean molecular weight, $\mu = 0.6$, and gas constant $\Re = k_B/m_p$, thereby assuming full ionization even in the coldest layers of our simulations. Magnetic diffusivity

TABLE 1
UNITS OF PHYSICAL QUANTITIES

Physical Quantity	Unit	Real Value
Length	$L = 2\tilde{\Lambda}_p$	5.4×10^7 cm
Velocity	$V_0 = \tilde{C}_{Sp}$	11.0 km s ⁻¹
Time	$2\tilde{\Lambda}_p/\tilde{C}_{Sp}$	49 s
Density	ρ_p	2.7×10^{-7} g cm ⁻³
Pressure	$\rho_0 V_0^2 = \gamma P_p$	3.33×10^5 dyn cm ⁻²
Temperature	T_p	5100 K
Magnetic field	$(\rho V_0^2)^{1/2}$	570 G

and viscosity are neglected since they are generally unimportant over the timescale of 1 hr in which our flux emergence takes place.

Thermal conduction is absent from our treatment primarily because its effects fall outside of our focus, the magnetically driven dynamics of flux emergence. Moreover, its correct inclusion would require the inclusion of radiation and coronal heating, between which conduction is often intermediary. An accurate treatment of radiation is very complicated since emergence brings the plasma from an optically thick regime to an optically thin one through the very complicated intermediate regime (Stein & Nordlund 1998). Furthermore, it is difficult to derive a physically meaningful model for the spatial distribution of coronal heating. Without some kind of heating, our simulation could not include a corona. We omitted all three of these processes, so any atmospheric structure in hydrostatic balance will be in steady state. This provides a reasonable setting for our dynamical simulation of flux tube emergence.

Quantities are rescaled using a length scale L , velocity V_0 , and mass density ρ_0 , defined with respect to photospheric values. The scales are taken to be $L = 2\tilde{\Lambda}_p = 540$ km, $V_0 = \tilde{C}_{Sp} = 11.0$ km s⁻¹, and $\rho_0 = \rho_p = 2.7 \times 10^{-7}$ g cm⁻³, where the subscript p denotes a photospheric value and tildes indicate quantities defined using the mean molecular weight $\mu = 0.6$ instead of its actual photospheric value; $\tilde{\Lambda}_p = 1.67\Re T_p/g$ and $\tilde{C}_{Sp} = (1.67\gamma\Re T_p)^{1/2}$ are the effective pressure scale height and sound speed at a photospheric temperature $T_p = 5100$ K (see below). Rescaling all quantities using L , V_0 , and ρ_0 leads to dimensionless variables that are advanced by our simulation; the most important scalings are listed in Table 1. The dimensionless variables satisfy equations (1)–(4), with the dimensionless gravity $g' = gL/V_0^2 = 2/\gamma$.

The rescaled differential equations (1)–(4) are time advanced with a modified Lax-Wendroff scheme that has a second-order accuracy in both time and space (Magara 1998).

2.2. The Model

2.2.1. Initial Conditions

The initial configuration of the simulation consists of a stratified background atmosphere in which a horizontal tube of twisted flux is embedded (see Fig. 1). The background atmosphere is defined by prescribing a continuous temperature distribution intended to represent the actual solar atmosphere. The temperature distribution is broken into four zones representing the subphotosphere ($z < z_p \equiv 0$), the photospheric layer ($z_p < z < z_t$), the low

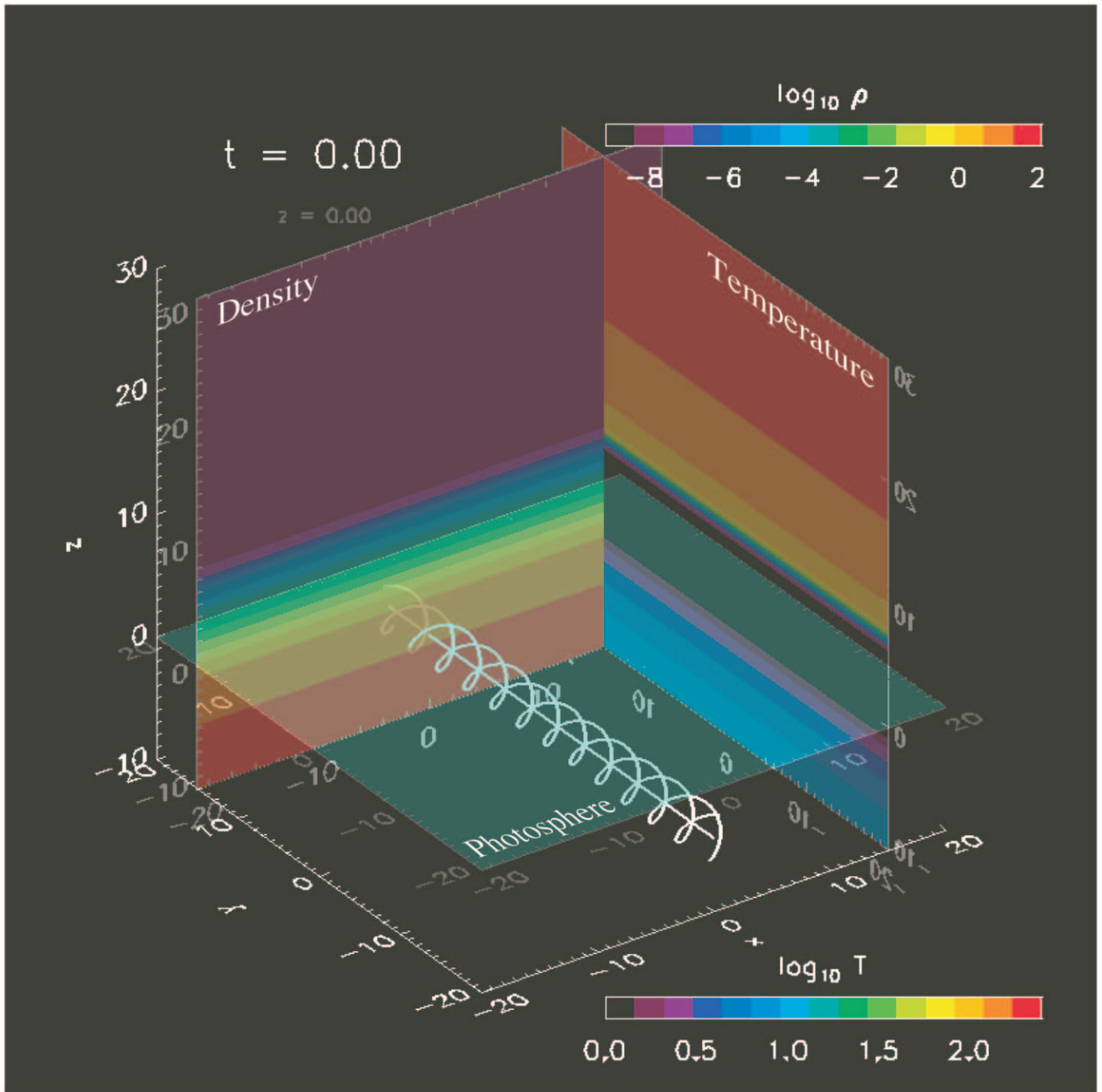


FIG. 1.—(a) Initial state of the simulation. A bundle of white lines shows a magnetic flux tube located below the photosphere. A horizontal color map represents the photospheric plane, and the two vertical color maps show the height variation of gas density and temperature, respectively. (b) Initial distribution of physical quantities along the z -axis, such as the gas pressure (Pg), density (ρ), temperature (T), and magnetic pressure provided by a magnetic flux tube (Pm). Temperature is plotted linearly against the right axis, and the other quantities are plotted logarithmically against the left axis.

corona ($z < z_{\text{cor}}$), and the high corona ($z > z_{\text{cor}}$). The sub-photosphere is a superadiabatic polytrope with temperature gradient $|dT/dz| = S_a |dT/dz|_{\text{ad}}$. Previous investigations (Magara 2001) showed that the choice $S_a = 1.025$ produces convective motions whose velocities are comparable to those predicted by mixing-length theory (Böhm-Vitense 1958; Stix 1991, p. 194). The temperature gradient, as well as gravity $g(z)$, decreases smoothly to zero at the bottom boundary.

The photospheric layer is intended to represent the region of relatively constant temperature, $T \sim 6500$ K, extending roughly 2000 km from the continuum $\tau = 1$ level in model C of Vernazza, Avrett, & Loeser (1981, hereafter VAL). Since the VAL model includes (among many other things) self-consistent ionization, its pressure scale height, $\Lambda_p \simeq 150$ km, is roughly half that of our model, $\Lambda_p = 270$ km. The principal dynamical effect of the entire layer is that the density drops by more than 6 orders of magnitude across it. In

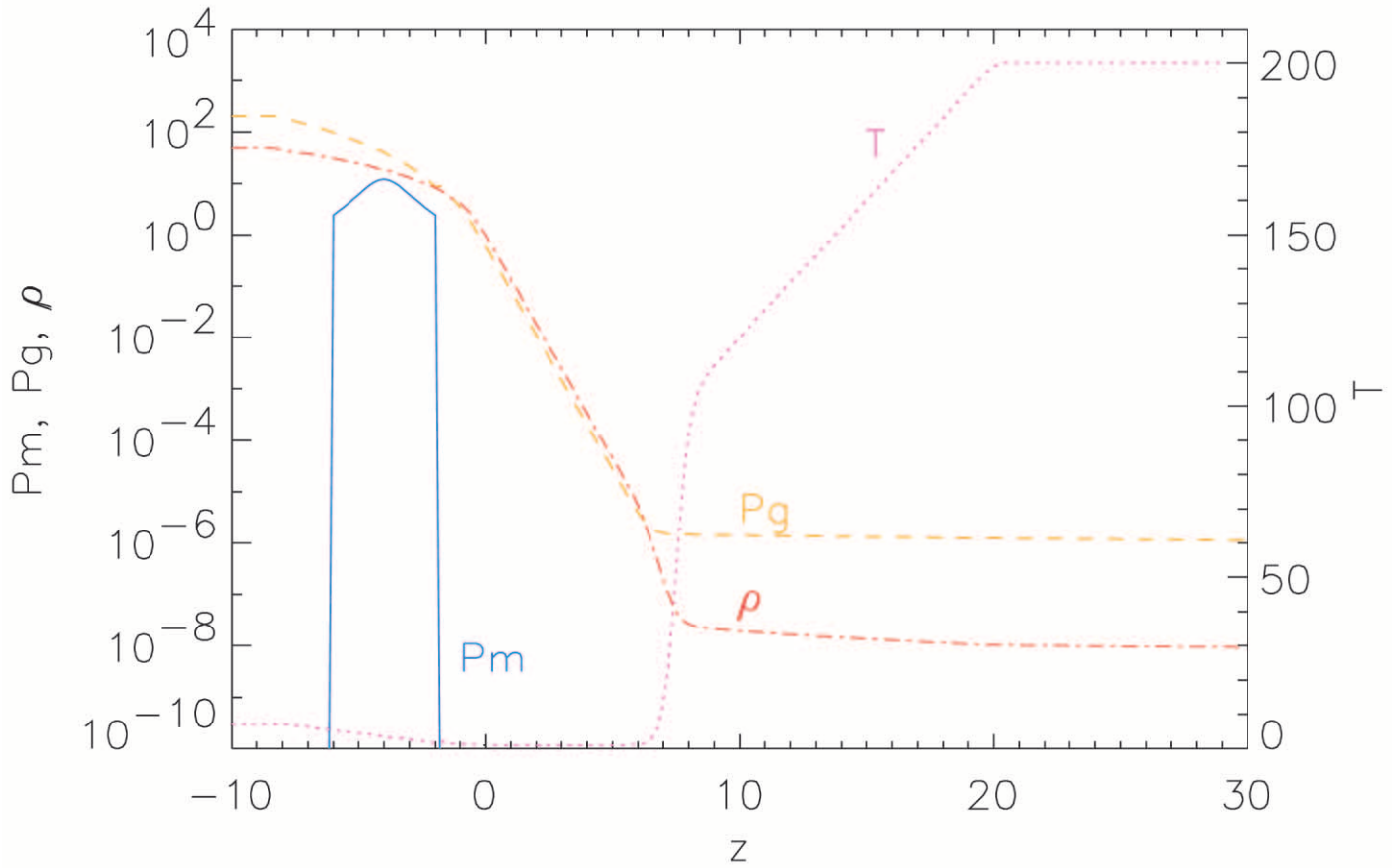


FIG. 1.—Continued

order to match this drop, thereby including a similar column density, our model requires a slightly cooler photospheric layer, $T_p = 5100$ K, which is roughly twice as thick, $z_t = 7.5L = 4050$ km.

From the photospheric value, temperature increases steeply to $T_c = 100T_p = 510,000$ K within a very narrow chromosphere and transition region. Above this the temperature increases linearly to its final value of $2T_c = 200T_p = 1.02 \times 10^6$ K within the low corona and retains this value throughout the high corona. The complete four-zone temperature model is shown in Figure 1b and given explicitly by

$$\begin{aligned}
 T(z) &= T_{\text{conv}} \quad (z < z_{\text{conv}}), \\
 T(z) &= T_p - S_a \left| \frac{dT}{dz} \right|_{\text{ad}} f(z) \quad (z_{\text{conv}} \leq z < z_p), \\
 T(z) &= T_p + (T_c - T_p) \left\{ \frac{1}{2} \left[\tanh\left(\frac{z - z_t}{w_t}\right) + 1 \right] \right\} \\
 &\quad \times (z_p \leq z < z_t), \\
 T(z) &= \left(T_p + (T_c - T_p) \left\{ \frac{1}{2} \left[\tanh\left(\frac{z - z_t}{w_t}\right) + 1 \right] \right\} \right) \\
 &\quad \times \left(\frac{z - z_t}{z_{\text{cor}} - z_t} + 1 \right) \quad (z_t \leq z < z_{\text{cor}}), \\
 T(z) &= \left(T_p + (T_c - T_p) \left\{ \frac{1}{2} \left[\tanh\left(\frac{z - z_t}{w_t}\right) + 1 \right] \right\} \right) \\
 &\quad \times 2(z_{\text{cor}} \leq z), \tag{6}
 \end{aligned}$$

where the remaining values are $T_{\text{conv}} = 7.1 = 36,200$ K, $z_{\text{cor}} = 20L = 10,800$ km, $z_{\text{conv}} = -8L = -4320$ km, and $w_t = 0.5L = 270$ km. The function $f(z)$ shuts off the superadiabatic temperature gradient in the vicinity of $z = 0$; its explicit form is

$$f(z) = \frac{1}{4} \ln \left\{ \frac{\cosh(2z_p)}{\cosh[2(z - z_p)]} \right\} + \frac{z}{2}. \tag{7}$$

From the prescribed temperature distribution (6) and the rescaled ideal gas law

$$\rho(z) = \frac{\gamma P(z)}{T(z)}, \tag{8}$$

the pressure distribution can be found by requiring hydrostatic balance

$$P(z) = P_p \exp \left[- \int_{z_p}^z \frac{2}{T(z')} dz' \right], \tag{9}$$

in terms of the rescaled temperature $T(z)$. This completely specifies the initial background atmosphere, shown in Figure 1b. By itself, the atmosphere is an equilibrium solution of our model equations that omit radiation, heating, and thermal conductivity.

A straight magnetic flux tube parallel to the y -axis is initialized at a depth of $4L = 2160$ km beneath the photosphere. The magnetic field within the tube is given by a

Gold-Hoyle flux tube twisted in the left-handed sense:

$$\mathbf{B}(x, y, z) = B_0 \frac{-b(z - z_0)\hat{\mathbf{x}} + \hat{\mathbf{y}} + b(x - x_0)\hat{\mathbf{z}}}{1 + b^2\left([x - x_0]^2 + [z - z_0]^2\right)},$$

$$(x - x_0)^2 + (z - z_0)^2 < r_0^2, \quad (10)$$

where $(x_0, z_0) = (0, -4)$ is the axis. Outside of the radius, $r_0 = 2L = 1080$ km, the magnetic field vanishes and there is a skin current at this interface. The field lines are uniformly twisted, making one helical turn over the axial distance $2\pi/b = 3400$ km ($b = 1/L$). The magnitude of the magnetic field is $B_0 = 17.4(\rho_0 V_0^2)^{1/2} = 10^4$ G on-axis, providing $\Phi = 1.4 \times 10^{20}$ Mx of net axial flux.

The tube's internal pressure and density distributions are defined to be in mechanical equilibrium. Internal pressure is lower than external pressure by $\Delta p = 0.2B_0^2/8\pi$ so that the sum of gas pressure and magnetic pressure is continuous across the flux tube boundary. Even with the deficit, the tube is pressure dominated: $\beta = 3.3$ on-axis. The pressure gradient matches that of hydrostatic atmosphere, so therefore must the density, in order to maintain mechanical equilibrium; the internal temperature is therefore lower owing to the pressure deficit.

To initiate rise we impose, for a short time ($0 \leq t \leq t_0 = 5$), a velocity field to drive the middle part of the flux tube upward, given explicitly by

$$v_z(x, y, z, t) = \begin{cases} \frac{\pi}{4t_0} \left[\cos\left(2\pi\frac{y}{\lambda}\right) + 1 \right] \sin\left(\frac{\pi t}{2t_0}\right) & -\frac{\lambda}{2} \leq y \leq \frac{\lambda}{2}, \\ 0 & \text{otherwise,} \end{cases} \quad (11)$$

within the fixed volume $(x - x_0)^2 + (z - z_0)^2 \leq r_0^2$. The wavelength of the perturbation is $\lambda = 30L = 16,200$ km so that the simulation box contains a single upward portion.

2.2.2. Boundary Conditions

The initial conditions, and the basic equations, are symmetric with respect to 180° rotation about the z -axis accompanied by a reflection of the magnetic field vector. Under this operation, B_z , v_x , and v_y change sign while all other quantities are unchanged. We take advantage of this symmetry to advance only one-half the simulation domain, $(0, -100, -10) \leq (x, y, z) \leq (100, 100, 100)$, and provide a symmetric boundary condition at the $x = 0$ plane. We impose periodic boundary conditions at $y = \pm 100$, a free boundary condition at $x = 100$ and $z = 100$, and a fixed, impermeable boundary condition at $z = -10$ (the initial value of each physical quantity is held fixed). In addition, we place a nonstratified isothermal layer (zero-gravity layer) near the top and bottom boundaries as well as a wave-damping region near all the boundaries except for $x = 0$.

3. RESULTS

This section presents the results of a single simulation run using the geometry and equations described above. First we investigate the dynamical nature of magnetic field lines when they emerge into the atmosphere. We then focus on the injection of the magnetic energy and magnetic helicity into the atmosphere. Since the injection of those quantities is related to the plasma motion at the base of the atmo-

sphere, we study the characteristics of gas flow around the photospheric magnetic polarity region.

3.1. Dynamical Nature of Emerging Field Lines

Figures 2a–2e show the temporal development of three magnetic field lines that initially compose a Gold-Hoyle force-free flux tube. Each figure presents three different views: the top, perspective, and side views. These views are shown at $t = 0$ (Fig. 2a), 10 (Fig. 2b), 20 (Fig. 2c), 30 (Fig. 2d), and 40 (Fig. 2e). The vertical velocity v_z and vertical magnetic field B_z throughout the $z = 0$ plane are indicated using colors and contours, respectively. The three field lines are selected by the intersection point where they initially cross the $y = 0$ plane. The red line, called the *central* field line, crosses $(x, y, z) = (0, 0, -4)$, which is the axis of the initial tube. The orange line, crossing initially at $(x, y, z) = (0, 0, -2.4)$, is called the *upper* field line, and the purple line, crossing initially at $(x, y, z) = (0, 0, -4.8)$, is called the *lower* field line.

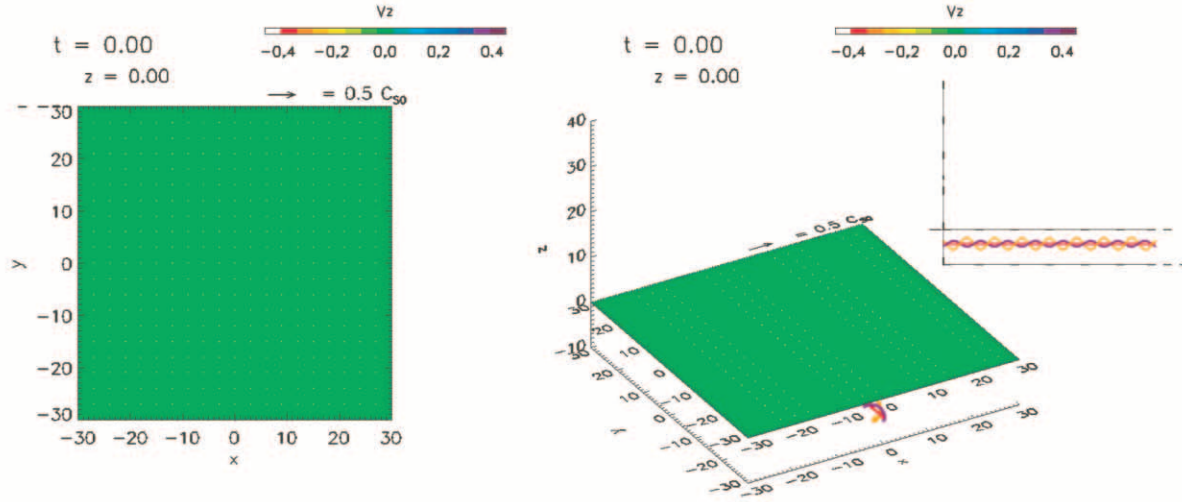
All three intersection points start to rise after the vertical motion is imposed (see eq. [11]). All the intersection points move along the z -axis because of the antisymmetry of the velocity field under 180° rotation about the z -axis [$v_x(0, 0, z, t) = v_y(0, 0, z, t) = 0$]. Their motion along the z -axis with time is displayed in Figure 3a, where dotted, dashed, and dot-dashed lines represent the central, lower, and upper field lines, respectively. The time derivative of the rise curves in Figure 3a yields the vertical velocity of intersection points in the Lagrangian frame. The time variation of this velocity is shown in Figure 3b.

The rise curves in Figures 3a and 3b show clearly the distinct character of evolution undergone by each of the three field lines. The upper field line simply continues to rise after emerging into the photosphere, and its rise velocity tends to increase with time. The lower field line rises through the convective layer at first, but later it becomes almost static and never emerges into the photosphere within the $y = 0$ plane. On the other hand, the central field line shows a more complicated behavior than the other two. According to Figure 3a, the central field line does emerge into the photosphere around $t = 16$, but it does not rise continuously after that. Figure 3b shows that the vertical velocity of the central field line tends to decrease with time ($16 \leq t \leq 28$), causing this field line to remain close to the photosphere during that time. This tendency changes around $t = 30$, when the central field line starts to rise, and its rise velocity increases rapidly in the subsequent evolution ($32 \leq t$).

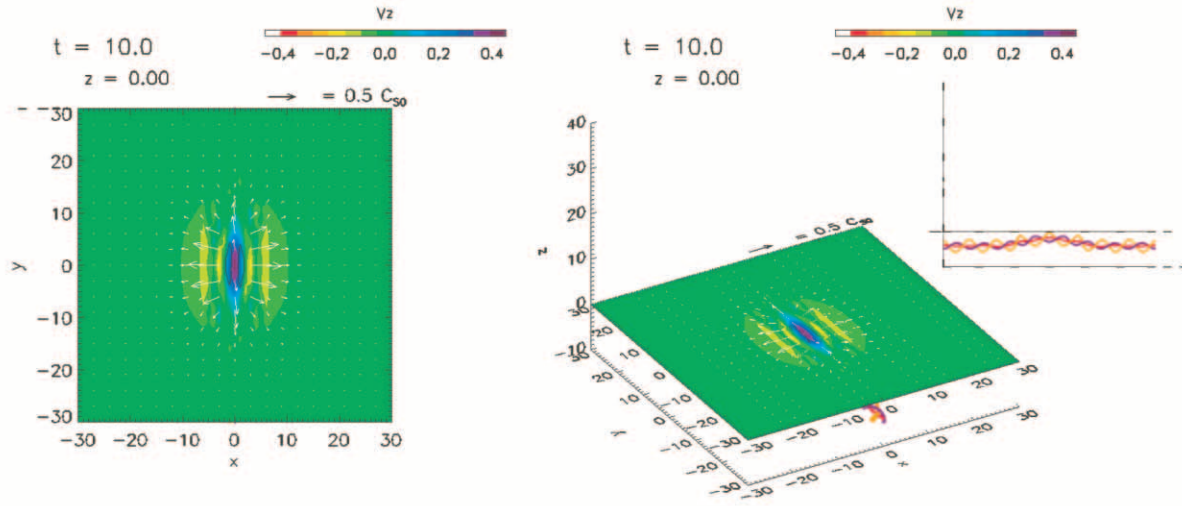
More details of the physics in individual field lines are shown in Figure 4. Snapshots of the emerging field lines from four times, $t = 18, 26, 32, 38$ (Figs. 4a, 4b, 4c, and 4d), are each shown from four different views. The snapshots show the velocity field on the upper and central field lines. Below the snapshots are two graphs showing how the vertical component of the force densities, the gas and magnetic pressure gradients, the magnetic tension, and the gravitational force are distributed along the upper (*upper graph*) and central (*lower graph*) field lines. The horizontal axis of those graphs is given by a signed length of field line, where $s = 0$ corresponds to the middle of the field line.

The upper field line undergoes the simplest evolution. The snapshots in Figures 4a–4d show that its crest always has an upward velocity and that plasma continuously drains downward from that point. According to the force

a)



b)



c)

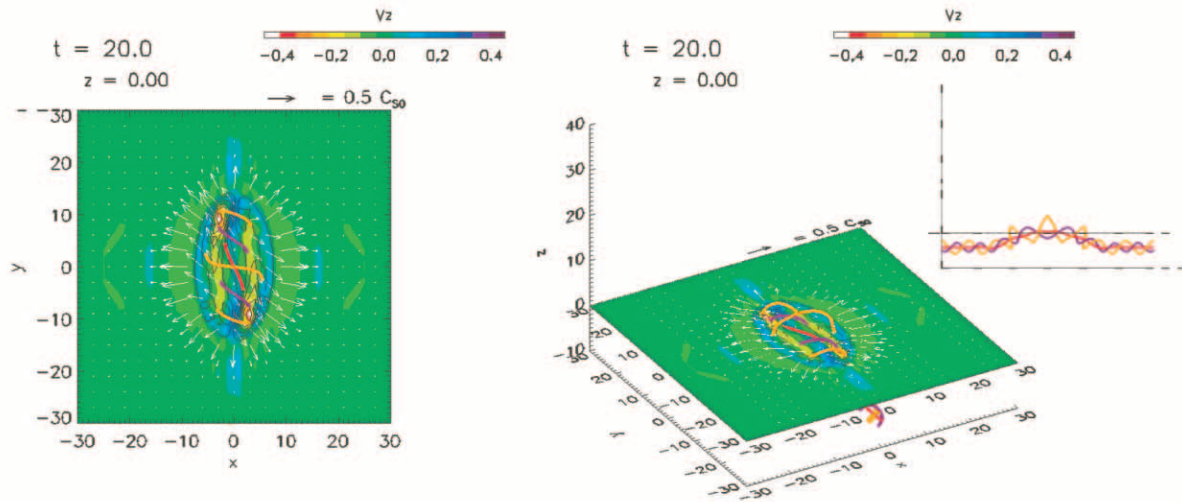
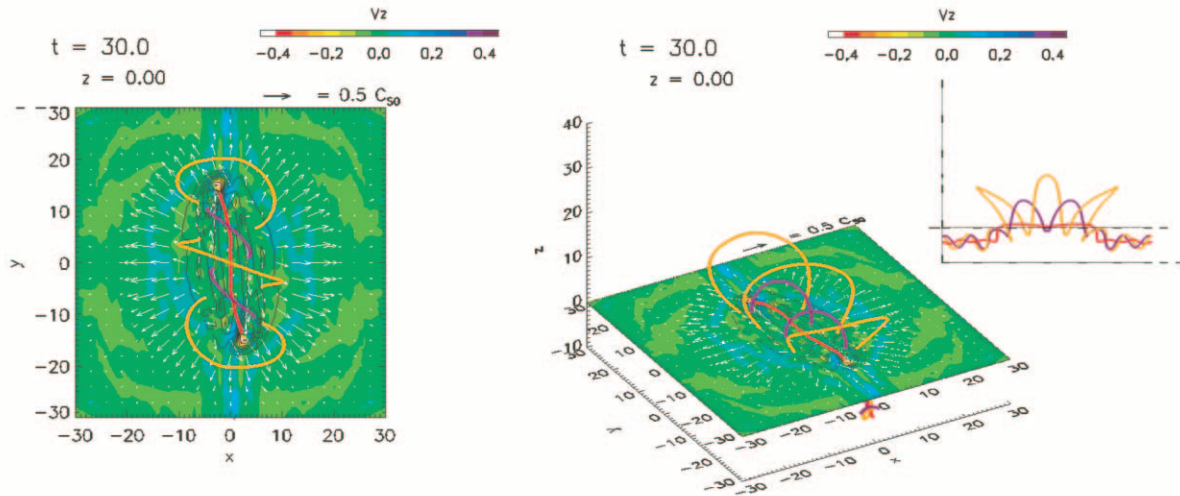


FIG. 2.—(a) Snapshots taken at $t = 0$, showing the top view (*left panel*), perspective view (*right panel*), and side view (*smaller panel at the top right corner of the perspective-view panel*). Field lines are represented by three colored lines, such as red, orange, and purple lines. A color map shows the vertical velocity, while contours and arrows on this map represent vertical magnetic flux and horizontal velocity field, respectively. (b) $t = 10$. (c) $t = 20$. (d) $t = 30$. (e) $t = 40$.

d)



e)

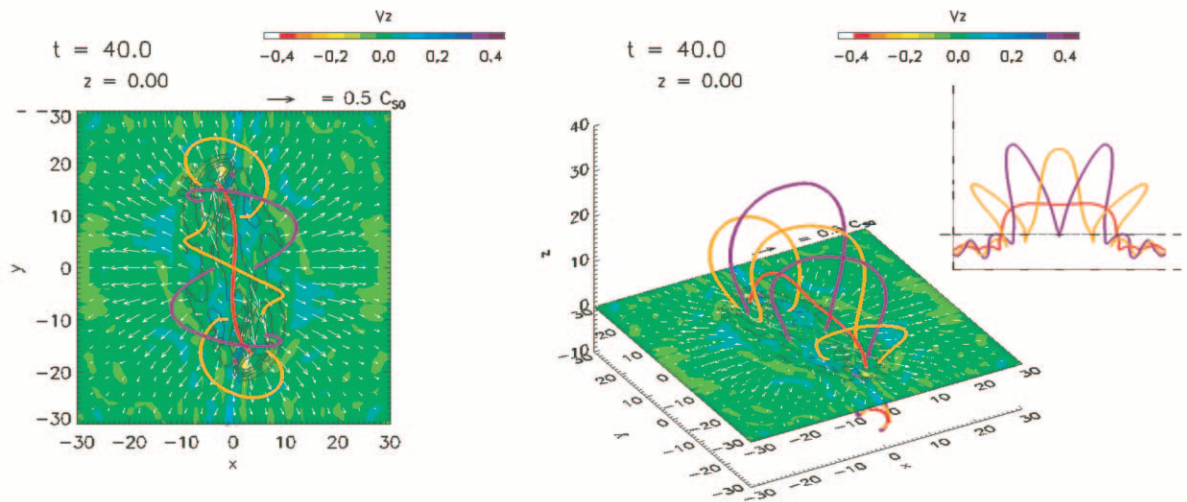


FIG. 2.—Continued

distribution, the main role in driving the upper field line upward is played by the magnetic pressure force. This upward force is principally opposed by the gravitational force at the early phase, although later the magnetic tension force also contributes as a downward force. The draining of plasma from the crest of the field line reduces the gravitational force, which helps the magnetic pressure force lift the field line. This in turn enhances the downflow of plasma from the crest. Such a positive feedback makes the upper field line expand continuously into the outer atmosphere. In other words, the magnetic buoyancy instability (Parker instability) works efficiently on the upper field line.

The behavior of the upper field line described above explains the physical process causing the continuous rise of emerging field lines. The essential part of this process is a draining of plasma from the ascending part of the field line. This weakens the gravitational force and enables the magnetic pressure force to drive the field line upward. If the plasma does not drain efficiently, then the field line is under the control of the downward gravitational force, which inhibits the vigorous rising.

The state of affairs is less obvious for the central field line. The snapshots in Figure 4a show that the plasma does move from the middle to the side. This motion is, however, relatively weak because the central field line is more nearly flat, reducing the plasma drainage. The gravitational force therefore remains effective and is almost balanced by the gas-pressure force. These two gaseous forces dominate the magnetic forces for a while (see the force distribution along the central field line in Fig. 4a), during which the central field line is prevented from expanding, or rather, a dip is formed in the middle of the field line (see Fig. 4b). The dip develops as mass accumulation proceeds, which eventually enhances the upward magnetic forces. Looking at the force distribution along the central field line in Figure 4c, we find that not only the gas-pressure force but also the magnetic forces work for supporting the dip against the gravitational force. Such an enhancement of magnetic forces changes the plasma motion on the central field line; that is, the plasma accumulated in the dip starts to rise, and then the whole field line enters an expansion phase during

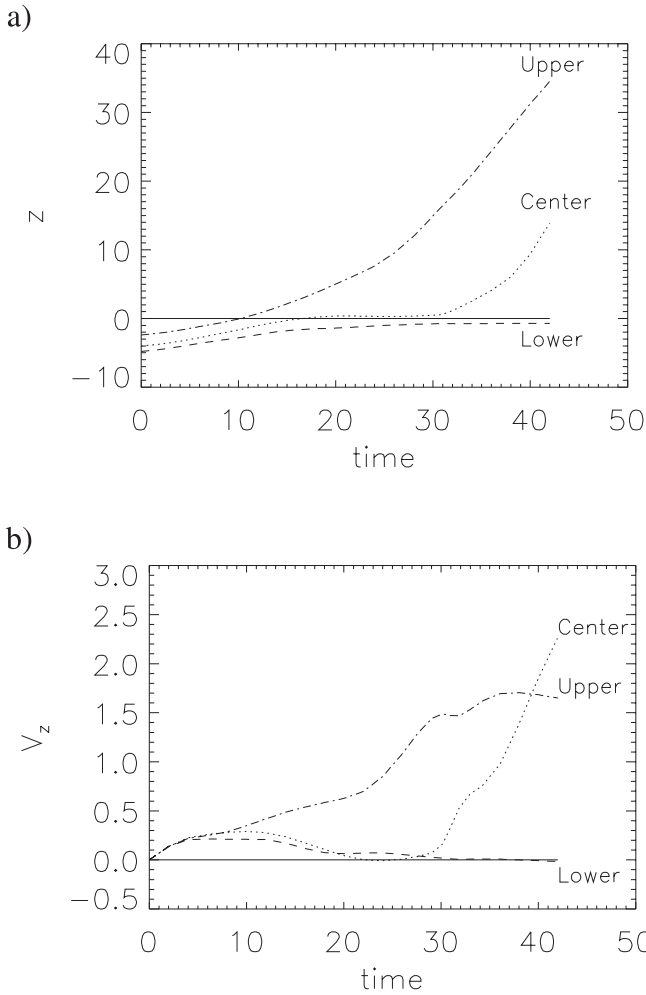


FIG. 3.—(a) Temporal displacement of the intersection point between the $y = 0$ plane and the field line shown in Fig. 2, which moves along the z -axis. (b) Time variation of the vertical velocity of the same intersection points as (a), obtained in a Lagrangian frame.

which the upward magnetic pressure force plays a dominant role (see the force distribution along the central field line in Fig. 4d).

In order to clarify how shape affects the evolution of emerging field lines, we introduce a model in which plasma flows steadily along a field line under uniform gravity. The field line prescribed in this model is given by a plane convex curve whose explicit form is

$$\begin{cases} X = a(\theta + \sin \theta) \\ Y = b(1 + \cos \theta) \end{cases} \quad \text{for } -\pi \leq \theta \leq \pi, \quad (12)$$

where X is a horizontal axis, Y is a vertical axis (directed upward), θ is a parameter, and (a, b) are positive constants (in the case of $a = b$, eq. [12] gives a cycloid). When we neglect the gas-pressure force along the field line, the kinematics of a plasma moving along the field line is determined by

$$v_s \frac{\partial v_s}{\partial s} = -g \frac{\partial Y}{\partial s}, \quad (13)$$

$$\frac{d}{dt} \ln \rho = -\frac{\partial v_s}{\partial s}. \quad (14)$$

Here $ds = (dX^2 + dY^2)^{1/2}$ is the infinitesimal length of the field line, $v_s(s)$ is the field-aligned velocity (time independent), $\rho(s, t)$ is the mass density along the field line (time dependent), and g is a constant gravitational acceleration. Next, we define s as a signed length:

$$\begin{aligned} s &= \int_0^\theta \sqrt{\left(\frac{dX}{d\theta'}\right)^2 + \left(\frac{dY}{d\theta'}\right)^2} d\theta' \\ &= \int_0^\theta \sqrt{(a^2 - b^2) \cos^2 \theta' + 2a^2 \cos \theta' + a^2 + b^2} d\theta', \quad (15) \end{aligned}$$

where $s = 0$ corresponds to the middle of the field line, about which the full field is symmetric. Because of this symmetry, $v_s(0) = 0$ and equation (13) may be integrated

$$v_s(s) = \sqrt{2g[2b - Y(s)]} \operatorname{sgn}(s). \quad (16)$$

Figure 5a shows three typical field lines given by equation (12) with $(a, b) = (1.0, 0.4)$, $(1.0, 1.0)$, and $(1.0, 1.5)$. For each field line, Figure 5b shows how v_s (upper panel) and its spatial derivative by s , v'_s (lower panel), are distributed along the field line (here we take $g = 1.2$). These figures indicate that the most convex field line ($a = 1.0, b = 1.5$) has the peak of v'_s at the crest while the least convex field line ($a = 1.0, b = 0.4$) has the peak at the side. According to equation (14), the density reduction occurs efficiently at the area where v'_s is large, which means that the crest of highly convex field lines and the side of weakly convex field lines are the area where the gas density decreases strongly. Since the decrease of gas density makes the magnetic buoyancy more effective, the crest of highly convex field lines rises strongly, thereby preserving the overall convex structure. On the other hand, in weakly convex field lines both sides tend to inflate, forming a dip in the middle of the field line where mass accumulates.

Those two kinds of behavior in emerging field lines are also observed in the dynamical simulation. Figure 5c displays the distribution of v_s and v'_s along the upper and central field lines. This figure shows that there is an enhancement of v'_s in the middle ($s = 0$) of the upper field line and at both sides ($s = \pm 1.5$) of the central field line. This suggests that the magnetic buoyancy works efficiently in the middle of the upper field line and at both sides of the central field line, which is reflected by the fact that the upper field line subsequently expands, keeping a convex shape, while the central field line forms a dip in the middle of the field line. Those results show that the emergence shape of field lines, or the ratio of their height to their footpoint distance, has a significant effect on their subsequent evolution.

Figure 6a displays how the vertical component of forces is distributed along the z -axis at $t = 36$, shown by a solid line for positive value (upward force) and by a dashed line for negative value (downward force). This figure shows that the subphotospheric region ($z < 0$) is dominated by the gas pressure and gravitational forces, both of which are almost comparable in size and much larger than magnetic forces. The dominance of plasma forces makes the magnetic buoyancy less effective for the field lines distributed below the photosphere. In order to make the magnetic buoyancy effective, it is necessary to lighten field lines by draining the plasma. However, since the field lines below the photosphere have a concave structure locally around the emergence area (see the purple field line in Figs. 2a–2e), the

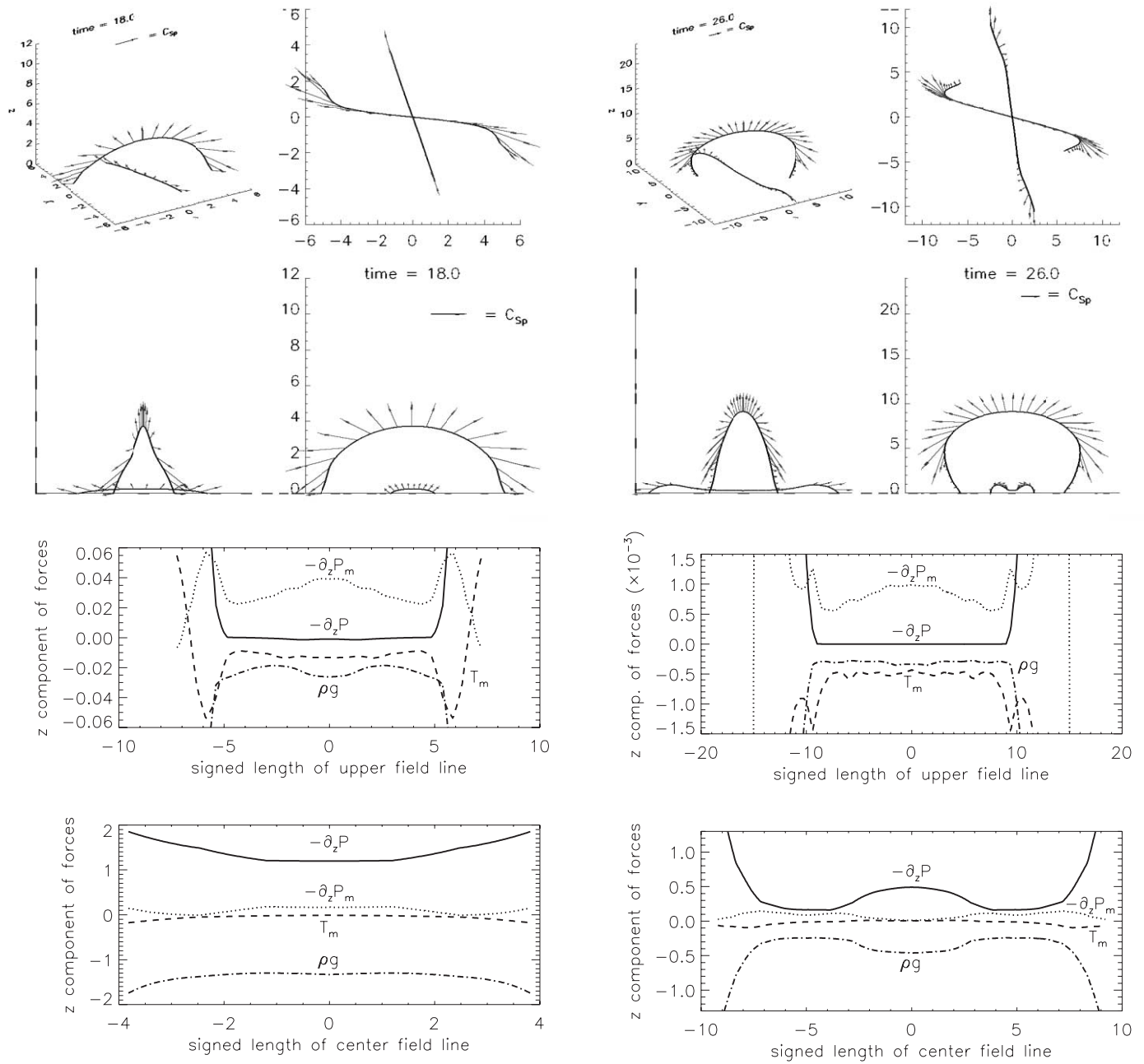


FIG. 4.—(a) Upper half is a set of four snapshots of the upper and central field lines taken at $t = 18$. Arrows show the velocity field on those field lines. Lower half is the distribution of vertical forces along the upper (*upper graph*) and central (*lower graph*) field lines obtained at $t = 18$. Solid, dotted, dashed, and dot-dashed lines represent the gas-pressure force, magnetic pressure force, magnetic tension force, and gravitational force, respectively. (b) $t = 26$. (c) $t = 32$. (d) $t = 38$.

plasma tends to slide down to the concave portion rather than drain from that portion. This geometric effect makes it hard to lift those field lines above the photosphere. Nevertheless, field lines that are initially located close to the axis of the flux tube can emerge into the photosphere because they originally have an almost flat shape so they are not strongly affected by the geometric effect. An examination of Figure 6a shows that the gravitational force is still almost balanced by the gas-pressure force just above the photosphere ($0 \leq z \leq 2$) and by the magnetic tension force in higher regions ($3 \leq z \leq 4$), which makes field lines distributed in $0 \leq z \leq 4$ move slowly. Above $z = 4$, there is a

region where the magnetic pressure force plays a dominant role in driving field lines upward. Figure 6b shows a set of snapshots of three emerging field lines located in the lower atmosphere, taken at $t = 36$.

Before closing this section, we should mention that our results concerning the evolution of emerging field lines are based on the assumption that the plasma evolves adiabatically and a plasma flow obeys an antisymmetry with respect to the z -axis. It is likely that certain features in the evolution would differ under more realistic assumptions. For example, asymmetric heating inside a magnetic loop could drive unidirectional flows. A study including those factors is

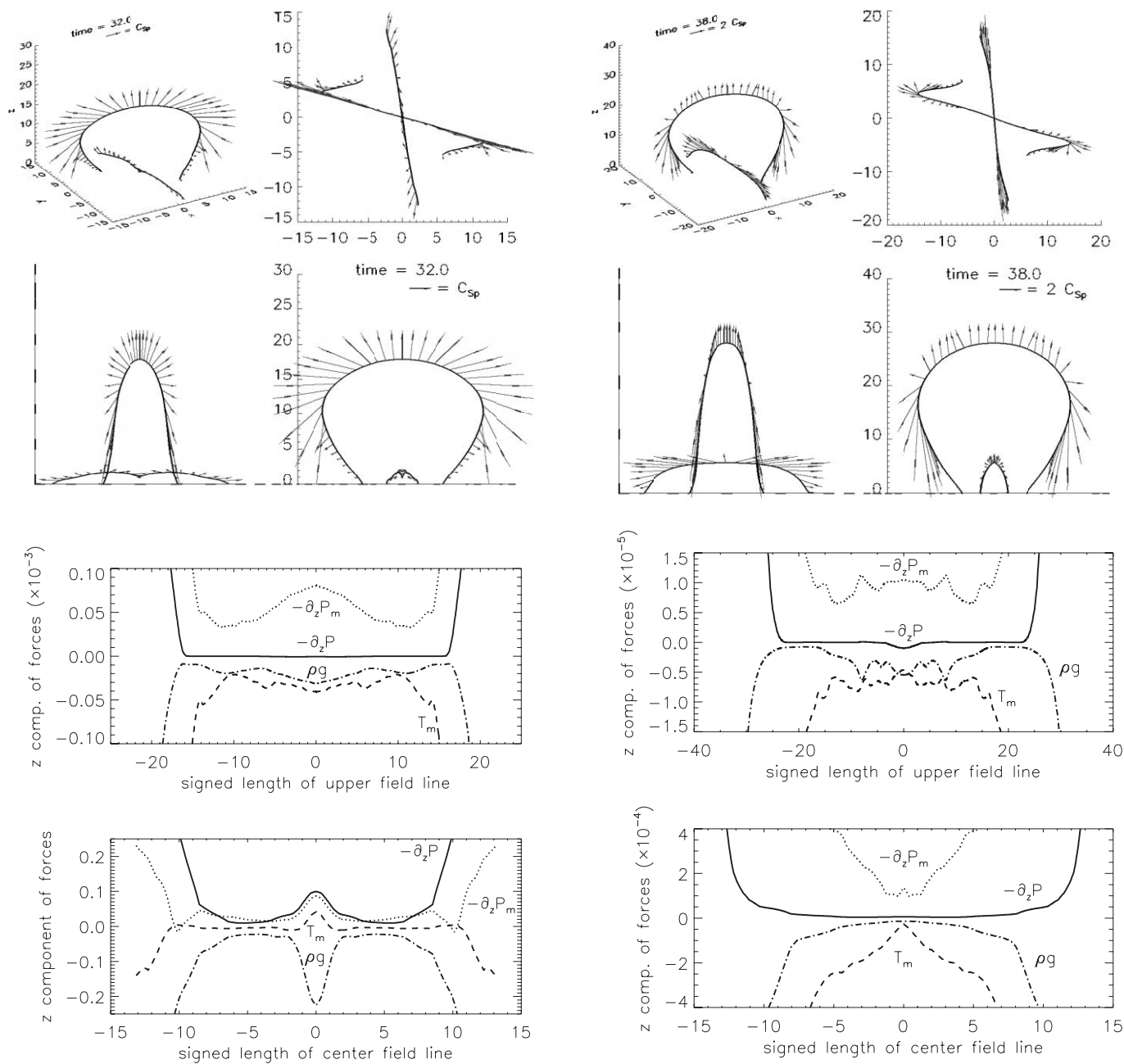


FIG. 4.—Continued

necessary, especially to see the long-term evolution of emerging field lines.

3.2. Injection of Magnetic Energy and Magnetic Helicity into the Atmosphere

The magnetic energy and magnetic helicity in the coronal field are given by the integrals

$$E_M(t) = \int_{z \geq 0} \frac{B(t)^2}{8\pi} dV, \quad (17)$$

$$H_M(t) = \int_{z \geq 0} \mathbf{A}(t) \cdot \mathbf{B}(t) dV, \quad (18)$$

where \mathbf{A} is a vector potential for \mathbf{B} . The magnetic helicity

H_M defined by equation (18) will become the gauge-invariant relative magnetic helicity (Berger & Field 1984; Finn & Antonsen 1985) when the vector potential is given by (DeVore 2000)

$$\mathbf{A}(x, y, z, t) = \mathbf{A}_C(x, y, 0, t) - \hat{\mathbf{z}} \times \int_0^z \mathbf{B}(x, y, z', t) dz'. \quad (19)$$

Here \mathbf{A}_C is a vector potential for the potential field that has the same photospheric distribution of vertical magnetic flux as \mathbf{B} . The exact form of \mathbf{A}_C is

$$\mathbf{A}_C(x, y, z, t) = \nabla \times \hat{\mathbf{z}} \int_z^\infty \phi_C(x, y, z', t) dz', \quad (20)$$

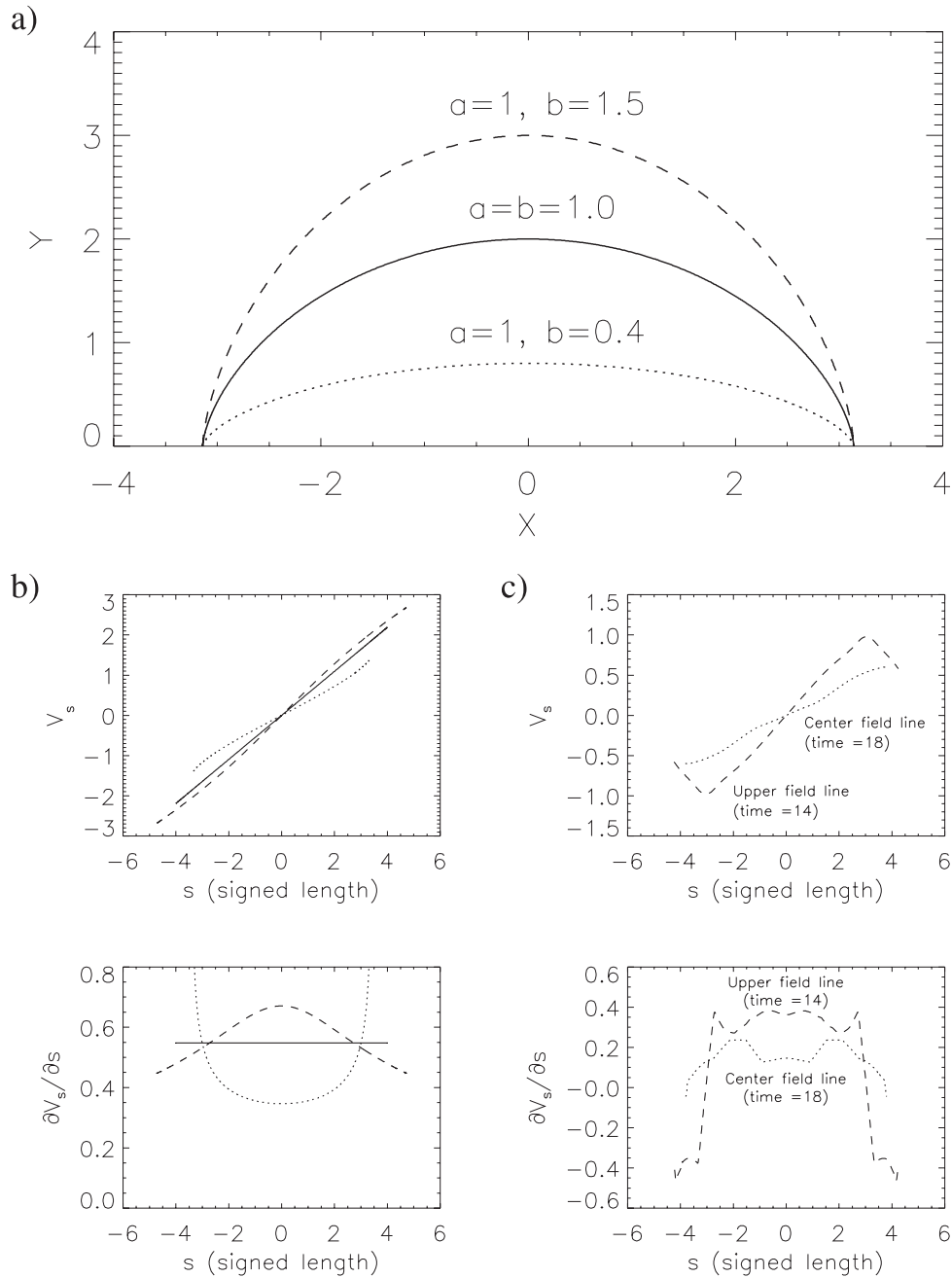


FIG. 5.—(a) Example of field lines described by eq. (12) with $a = b = 1.0$ (solid line), $a = 1, b = 1.5$ (dashed line), and $a = 1, b = 0.4$ (dotted line). (b) Distribution of field-aligned velocity (upper graph) and its spatial derivative (lower graph) along the field line shown in (a). Solid, dotted, and dashed lines show the cases of solid, dotted, and dashed field lines. (c) Same distribution as (b) except for the cases of the upper and central field lines obtained by the simulation.

where ϕ_C is a scalar potential for the potential field, given by

$$\phi_C(x, y, z, t) = \frac{1}{2\pi} \int_{z=0} \frac{B_z(x', y', 0, t) dx' dy'}{[(x - x')^2 + (y - y')^2 + z^2]^{1/2}}. \quad (21)$$

The Poynting flux of magnetic energy through the photosphere is

$$F_{M,z} = -\frac{1}{4\pi} \int_{z=0} (B_x v_x + B_y v_y) B_z dx dy + \frac{1}{4\pi} \int_{z=0} (B_x^2 + B_y^2) v_z dx dy. \quad (22)$$

The first term on the right-hand side of equation (22) represents the work done by horizontal motions and will be called the *shear term*. The second term, called the *emergence term*, would clearly vanish in the absence of vertical flows.

The magnetic helicity flux through the photosphere is

$$F_{H,z} = -2 \int_{z=0} (A_x v_x + A_y v_y) B_z dx dy + 2 \int_{z=0} (A_x B_x + A_y B_y) v_z dx dy, \quad (23)$$

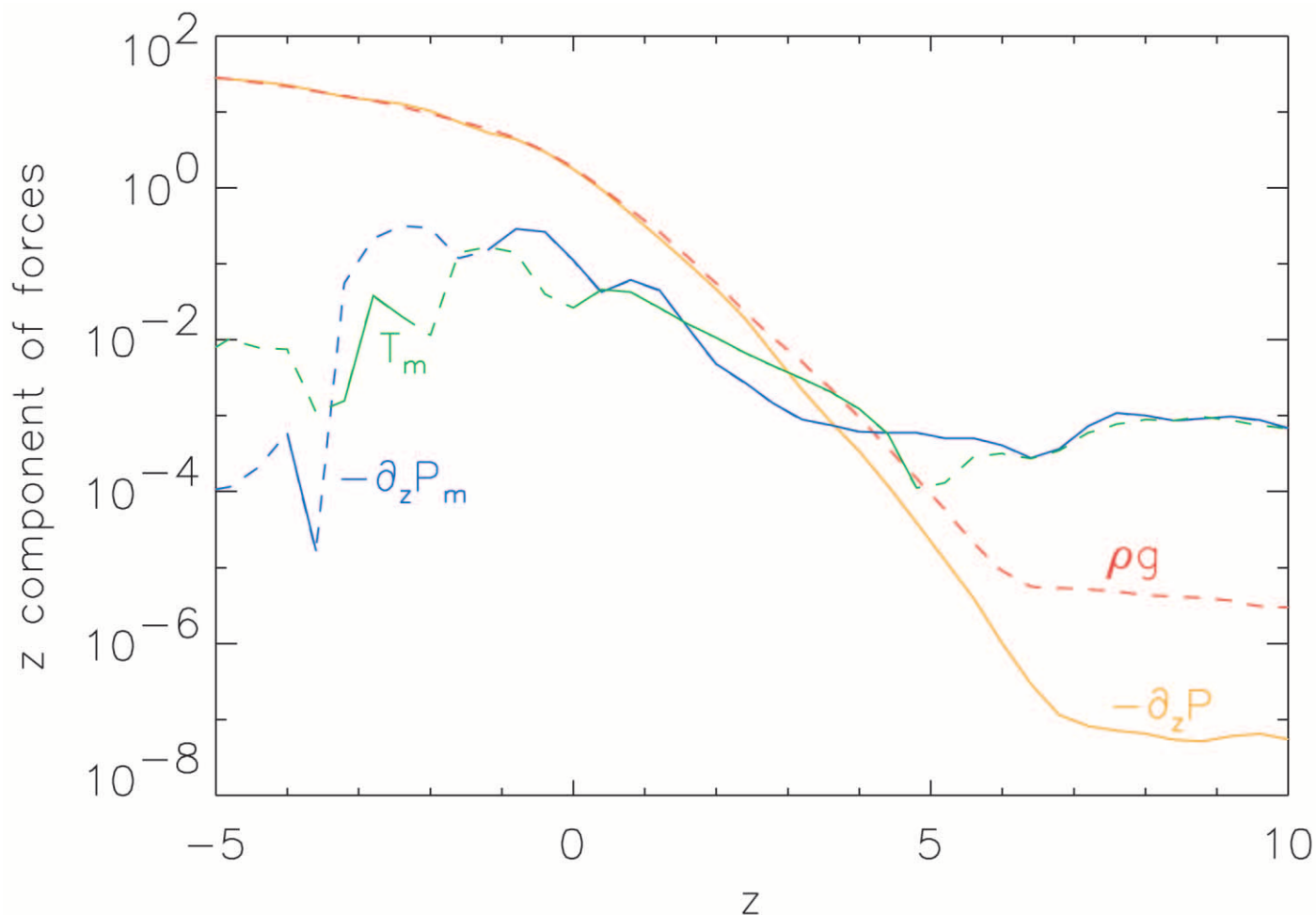


FIG. 6.—(a) Distribution of vertical forces (gas-pressure force, gravitational force, magnetic pressure force, and magnetic tension force) along the z -axis obtained at $t = 36$. Solid portion of lines shows the positive value (upward force), while broken portion shows the negative value (downward force). (b) Snapshots of three field lines emerging into the lower atmosphere, taken at $t = 36$. Arrows show the velocity field on those field lines.

where, once again, the first and second terms on the right-hand side are the shear term and the emergence term.

Figure 7 shows the time variation of the energy, helicity, and their respective fluxes beginning at $t = 10$, when the flux tube starts to emerge into the photosphere. Figures 7a and 7c show that both the magnetic energy and the magnetic helicity increase rapidly just after the emergence begins. Figures 7b and 7d indicate that both fluxes are dominated by the emergence term during the early phase and by the shear term later.

As is seen in Figure 2c, the central part of the flux tube (near the axis) emerges into the atmosphere around $t = 20$; this is when stronger field lines cross the photosphere. Until that time the strength of newly emerged field lines increases with time, causing a natural increase of the magnetic energy of the potential field (the magnetic energy of the emerging field also shows a similar tendency, although part of this energy is continuously converted into kinetic energy through magnetic buoyancy). After that time the strength of emerging field lines decreases with time, so the potential energy becomes saturated and even reduced at the late phase.

The twisted structure of magnetic field lines is an important factor in the cause of horizontal photospheric motions (see § 3.3). Even after $t = 20$ (the emergence of the central

flux tube) horizontal motions are driven by twist since the outer field lines are still more twisted than the stronger, central field lines. These magnetically driven motions contribute to injecting magnetic energy and magnetic helicity via the shear term (see Figs. 7b and 7d). While vertical motions directly carry the magnetic flux into the atmosphere to input the magnetic energy and magnetic helicity, horizontal motions driven by twisted field lines use shear Alfvén waves (torsional Alfvén waves) to input those quantities. The latter process is also studied by Manchester (2001), in whose work two-dimensional simulations of flux emergence across the photosphere are diagnosed and interpreted in terms of shear Alfvén waves.

By the late phase ($30 \leq t \leq 40$), the increases of magnetic energy and magnetic helicity have saturated. Figures 7a and 7c show the different manner of saturation for these two quantities. The magnetic energy decreases slightly, while the magnetic helicity continues to increase gradually. This difference results from the fact that even when the photospheric emergence is complete the upper portion of the atmosphere is evolving dynamically as magnetic energy is converted to kinetic energy. This conversion does not affect the magnetic helicity, which therefore continues to increase from the shear term. The continuing contributions of the shear term, even into the late phase, suggest a significant

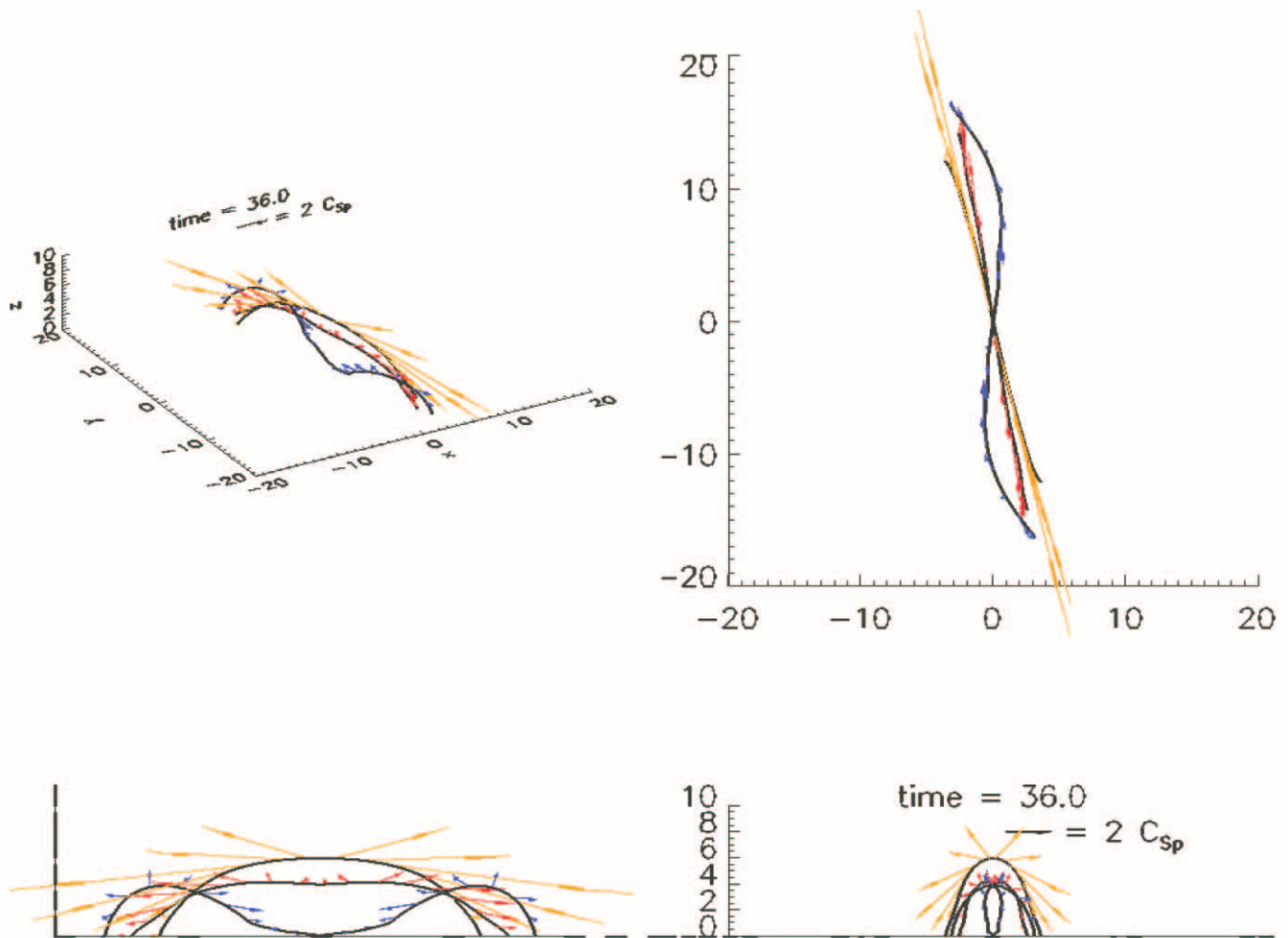


FIG. 6.—Continued

coupling between vertical magnetic flux and horizontal flow in the photosphere. Since the area of strong vertical magnetic flux forms a photospheric magnetic pole, we next investigate the characteristics of horizontal flow in the vicinities of these polarity regions.

3.3. Evolution of Photospheric Magnetic Polarity Region

Figure 8 shows the temporal development of the magnetic polarity region in the photosphere. Each subfigure consists of two panels. The larger shows a gray-scaled map of B_z , contours of v_z , and white arrows showing the horizontal velocity field, while the smaller includes a group of emerging field lines shown as black curves.

According to Figure 8a, the emergence starts with a simple bipole structure in which the positive polarity is to the left of the neutral line, the negative polarity to the right, and emerging field lines are almost perpendicular to the neutral line. Comparison to Figure 2b, from almost the same time, shows that there is a strong upflow around the neutral line and a weaker downflow to either side. This pattern is the result of plasma moving upward in the middle of emerging field lines and flowing downward along their legs and into their footpoints. The emergence also drives horizontal flows, shown by the arrows in Figures 8a–8d. The flow direction changes in accordance with the shape of emerging field line, so the inner field lines that emerge late rotate toward

the neutral line. This results in the flow direction changing from perpendicular to the neutral line toward parallel to the neutral line.

During emergence, the locations of the peak vertical field move apart along the axis of the tube (i.e., the y -axis). The peak positive (negative) pole moves in the $+\hat{y}$ ($-\hat{y}$) direction. There are also secondary local maxima that accompany the regions of opposite polarity. A secondary positive- (negative-) polarity region accompanies the negative (positive) peak. This process elongates each polarity in the y -direction and later forms a quadrupole structure (Fig. 8d). That quadrupole is composed of a main bipole, where opposite-polarity regions are connected to each other by the field lines that are almost aligned with the neutral line (these field lines are originally distributed near the axis of the flux tube), and a secondary dipole, where each polarity region is connected to the opposite-polarity region of the main dipole (see Fig. 8d).

The development of quadrupolar structure differs from the report of Magara & Longcope (2001), in which the final stage of emergence has a dipole structure rather than a quadrupole structure. The difference arises from the fact that the leg of the emerging Ω loop in the present simulation is more inclined to the photosphere. Since Magara & Longcope (2001) assigned a downward motion on all portions along the initial flux tube except for the middle emerging

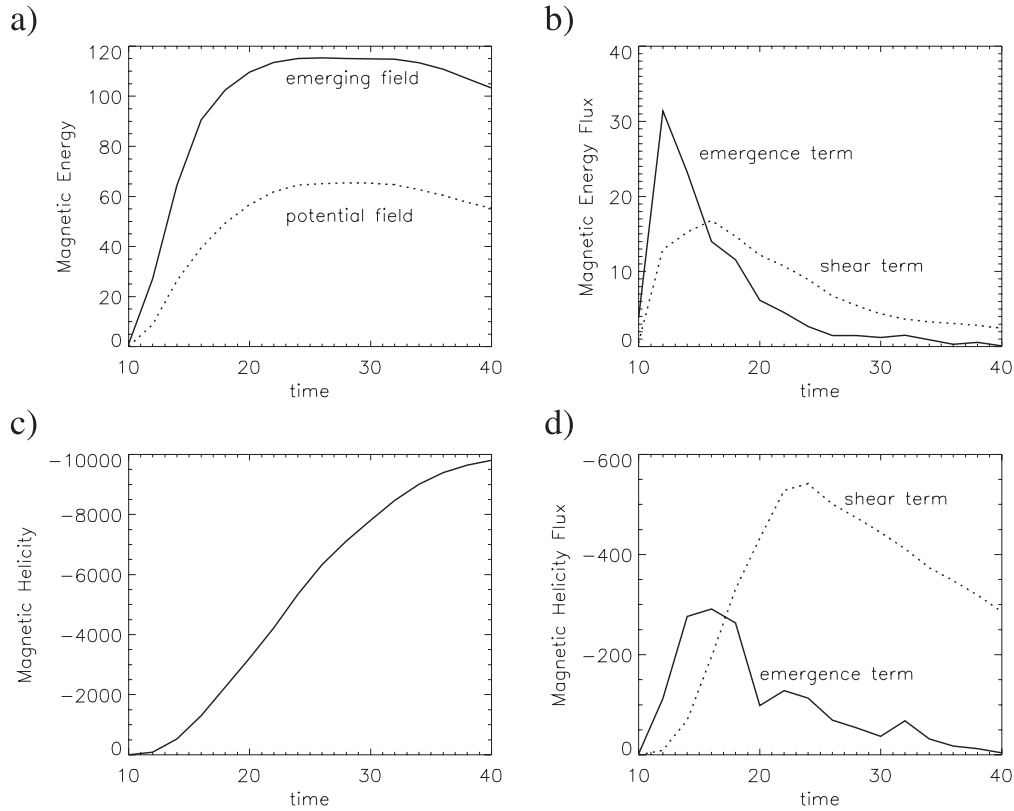


FIG. 7.—(a) Time variation of the magnetic energy stored in the atmosphere ($z \geq 0$). The solid line represents the energy of the emerging magnetic field, and the dotted line represents the energy of potential field that has the same photospheric distribution of vertical magnetic flux as the emerging magnetic field. (b) Time variation of the magnetic energy flux injected through the photosphere. Dotted and solid lines represent the first (shear term) and the second (emergence term) terms on the right-hand side of eq. (22). (c) Time variation of the magnetic helicity stored in the atmosphere ($z \geq 0$). (d) Time variation of the magnetic helicity flux injected through the photosphere. Dotted and solid lines represent the first (shear term) and the second (emergence term) terms on the right-hand side of eq. (23).

part, the leg of the emerging Ω loop becomes more vertical than in the present case, so the cross section of the loop in the photosphere comes close to a single round shape.

To further investigate the horizontal flow around the photospheric magnetic polarity region, we decompose the horizontal velocity into two components. The first component, \mathbf{v}_c , is the time derivative of the peak flux location, which is defined for the positive polarity

$$\mathbf{r}_c \equiv \frac{\int_{z=0} B_z(x, y, 0, t) \mathbf{r} dx dy}{\int_{z=0} B_z(x, y, 0, t) dx dy}$$

for $B_z(x, y, 0, t) > 0.95 \max[B_z(x, y, 0, t)]$, (24)

where $\mathbf{r}_c = (x_c, y_c)$ and $\mathbf{r} = (x, y)$ are position vectors within the photospheric plane. The second component, \mathbf{v}_r , is the fluid flow velocity relative to the peak.

In Figure 9a, a thick dashed line traces the position of the peak flux area from $t = 10$ to 40, and a black arrow shows the velocity of the peak flux area (\mathbf{v}_c) at $t = 10, 18, 28,$ and 40. Contours and light gray arrows represent the vertical magnetic flux and the relative velocity field (\mathbf{v}_r) around the peak flux area. Figure 9b shows the time variation of the distance between peak flux areas of positive and negative polarities, and Figure 9c indicates the time variation of the total amount of positive and negative magnetic flux penetrating the photosphere.

At the early phase of emergence, magnetic polarity regions are formed and developed through the continuous

emergence of new magnetic flux from the subphotosphere. Such a vigorous emergence causes a rapid increase of the magnetic flux (Fig. 9c), magnetic energy (Fig. 7a), and magnetic helicity (Fig. 7c). During this phase the area of the magnetic polarity region simply extends horizontally, as is indicated by the diverging pattern of horizontal flow at $t = 10$ in Figure 9a. Strong emergence almost stops after the axis of the flux tube emerges into the photosphere (around $t = 16$), and shortly thereafter the increase of magnetic flux saturates. In contrast to the early emergence phase, when a simple dipole structure is formed, the late phase is a deformation and fragmentation of the magnetic polarity regions, leading to a quadrupole structure. The relative velocity field during the late phase ($t = 28, 40$) in Figure 9a shows that a rotational flow appears around the peak flux area. The rotational flow twists the vertical magnetic field, which injects energy and helicity into the atmosphere. This effect provides a significant shear term contribution to both energy and helicity flux during the late phase, as shown in Figures 7b and 7d.

Color maps in Figures 10a–10h show the photospheric distribution of emergence and shear terms of magnetic energy and helicity fluxes at both the early ($t = 12$) and late ($t = 36$) phases of emergence. Contours on these maps represent the vertical magnetic flux. At the early phase, strong injection of magnetic energy and helicity by emergence is distributed around the neutral line (Figs. 10a and 10c), while strong injection by shearing motion occurs in intense flux

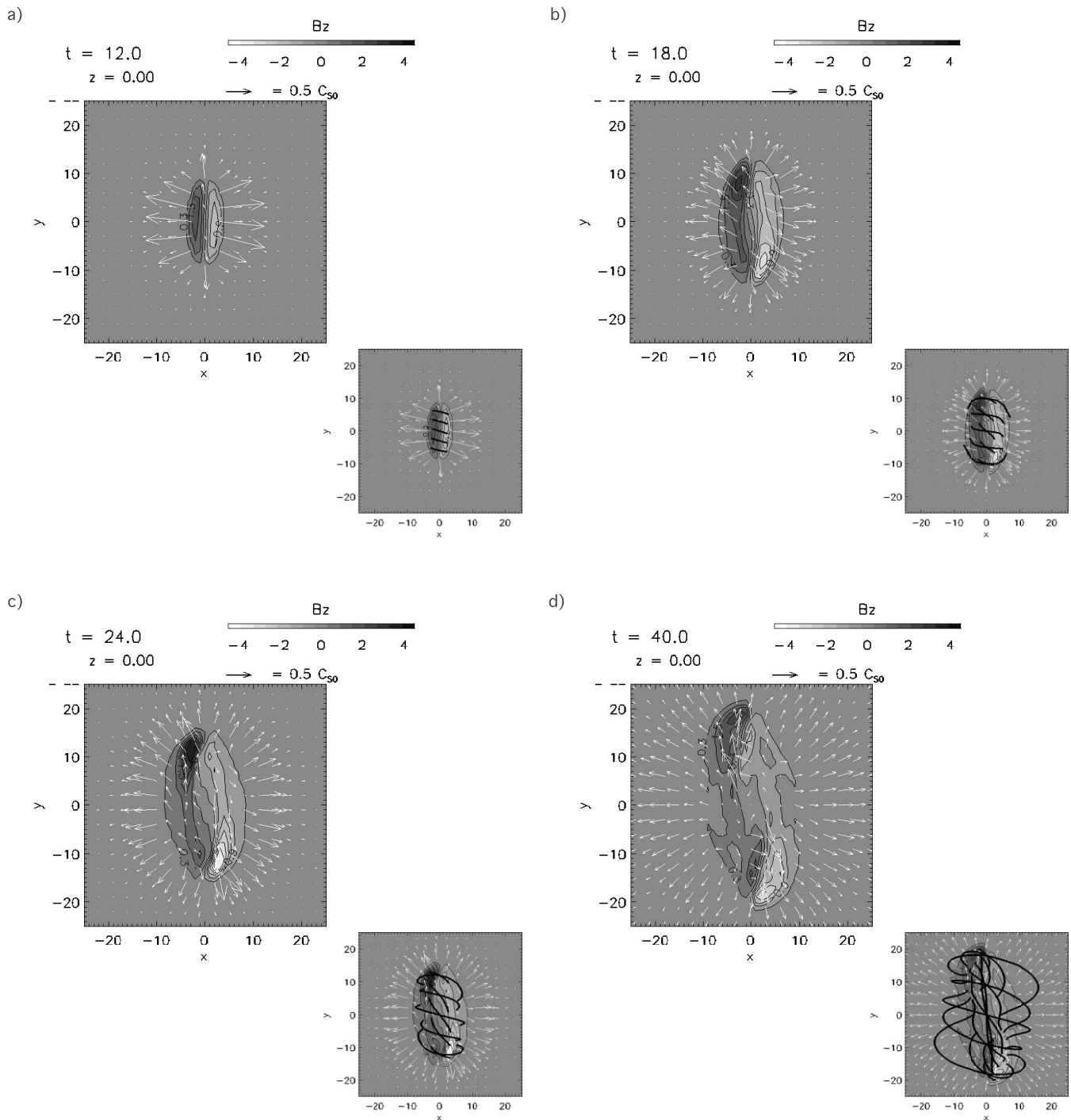


FIG. 8.—(a) Snapshots taken at $t = 12$, showing the top view without emerging field lines (*main panel*) and with emerging field lines (*smaller panel at the bottom right corner of the main panel*), which are represented by black lines. A gray-scaled map and contours on this map show vertical magnetic flux, while arrows on this map represent horizontal velocity field. (b) $t = 18$. (c) $t = 24$. (d) $t = 40$.

areas (Figs. 10b and 10d). According to Figure 10c, there is a dominant input of negative magnetic helicity by emerging motion (the original magnetic flux tube has a negative helicity); however, Figure 10d shows a significant input of positive and negative magnetic helicity by shearing motion. This comes from the fact that the horizontal flow takes a diverging pattern that shears the upper and lower parts of the magnetic polarity region in an opposite way; the flow is directed in the positive y -direction at the upper part and in

the negative y -direction at the lower part (see $t = 10$ in Fig. 9a).

There are two notable regions at the late phase: one is the neutral line between the main and subsidiary polarity regions, and the other is the peak flux area of the main polarity. The emergence panels, Figures 10e and 10g, show that the positive input of magnetic energy and helicity occurs around the neutral line (“positive input” here means increasing the amount stored in the atmosphere) and negative input

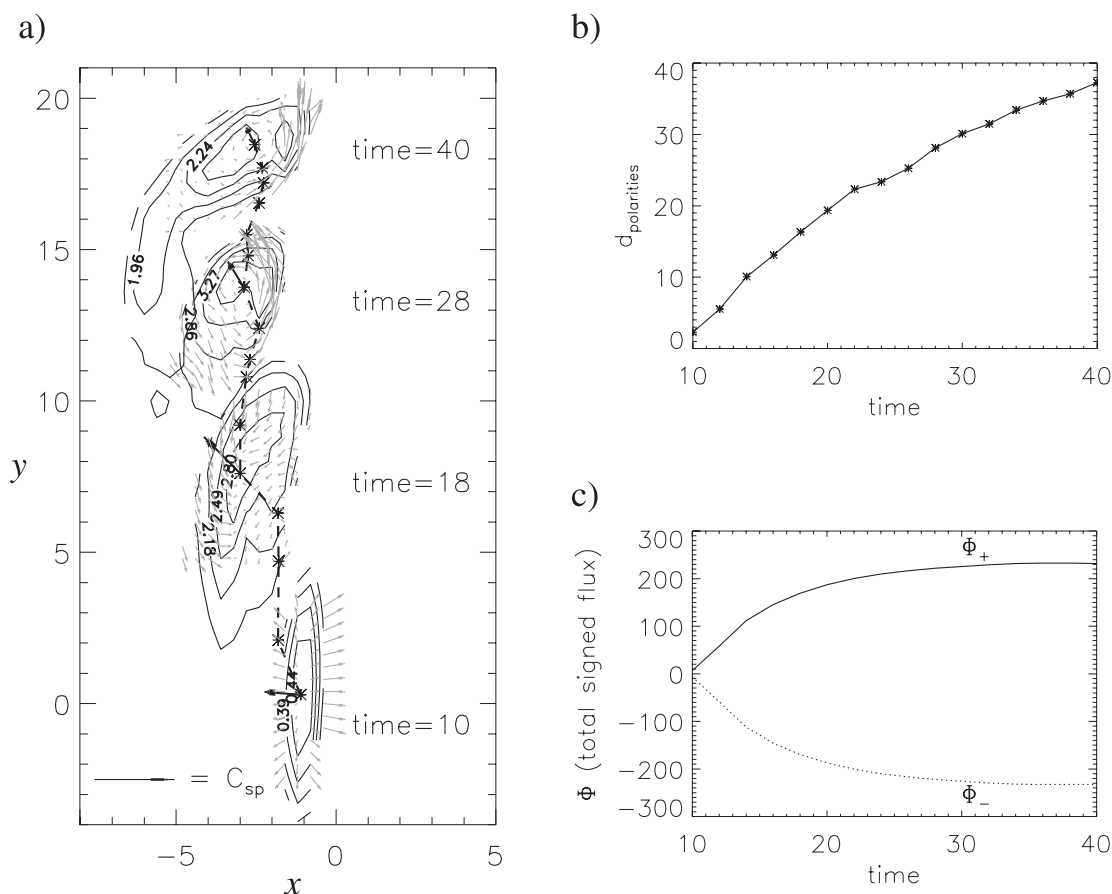


FIG. 9.—(a) Temporal development of positive magnetic polarity region in the photosphere. A thick dashed line traces the peak flux area of positive magnetic polarity from $t = 10$ to $t = 40$. Contours show vertical magnetic flux, while the black arrow represents the velocity of peak flux area. Gray arrows show the velocity field relative to the velocity of peak flux area. These are obtained at $t = 10, 18, 28,$ and 40 . (b) Time variation of the distance between the peak flux areas of positive and negative polarities. (c) Time variation of the total amount of positive and negative magnetic flux in the photosphere.

occurs at the peak flux area. This reflects an upflow at the neutral line and a downflow around the peak flux area at the late phase of emergence (see Figs. 2*d* and 2*e*). On the other hand, Figures 10*f* and 10*h* show that the strong positive input of magnetic energy and helicity by shearing motion occurs around the peak flux area where the rotational flow (see $t = 28, 40$ in Fig. 9*a*) makes significant contributions to inputting those quantities into the atmosphere.

4. DISCUSSION

The foregoing sections show the dynamical nature of emerging magnetic field lines that compose a twisted flux tube. Analyses of these results show that field lines have one of two distinct evolutionary characters, depending on their initial positions inside the flux tube. This distinction in evolutionary character might have significant consequences for observed solar phenomena caused by emerging magnetic fields, such as arch filament systems (AFSs), U loops, prominences, helmet streamers, and sigmoids. It is premature, however, to make a direct comparison between the simulation results and those actual phenomena because most of the phenomena evolve under thermal conduction and radiation, which could not be accounted for in our simulation. Certain basic qualitative properties such as the shape and motion will not be grossly affected by conduction or radia-

tion and should be adequately predicted by our simulation results.

Figure 11 illustrates two kinds of models of emerging field lines categorized on the basis of their evolutionary character. The simulation shows that emerging field lines take the evolutionary path of a simple expansion if they emerge with a large aspect ratio (the ratio of their height to their foot-point distance); otherwise, field lines are inhibited from expanding and they show an undulating behavior. According to the kinematics of emerging field lines considered in § 3.1, the critical aspect ratio between the height and half-footpoint distance whereby emerging field lines are classified into two groups (expanding field lines and undulating field lines) is about 1. Expanding field lines continue to inflate their overall structure, keeping a simple convex shape in which a plasma goes upward in the middle and drains downward at both sides. On the other hand, undulating field lines wave up and down, and mass accumulates in the concave portion.

There are two possibilities for the subsequent evolution of an undulating field line: the concave portion either expands outward or sinks toward the photosphere after developing a dipped structure. More precisely, the state of undulating field lines is determined by the balance between the gravity exerted on the plasma sliding down to the concave portion and the repulsive magnetic forces. When the sliding is sufficiently strong, the gravity overcomes the

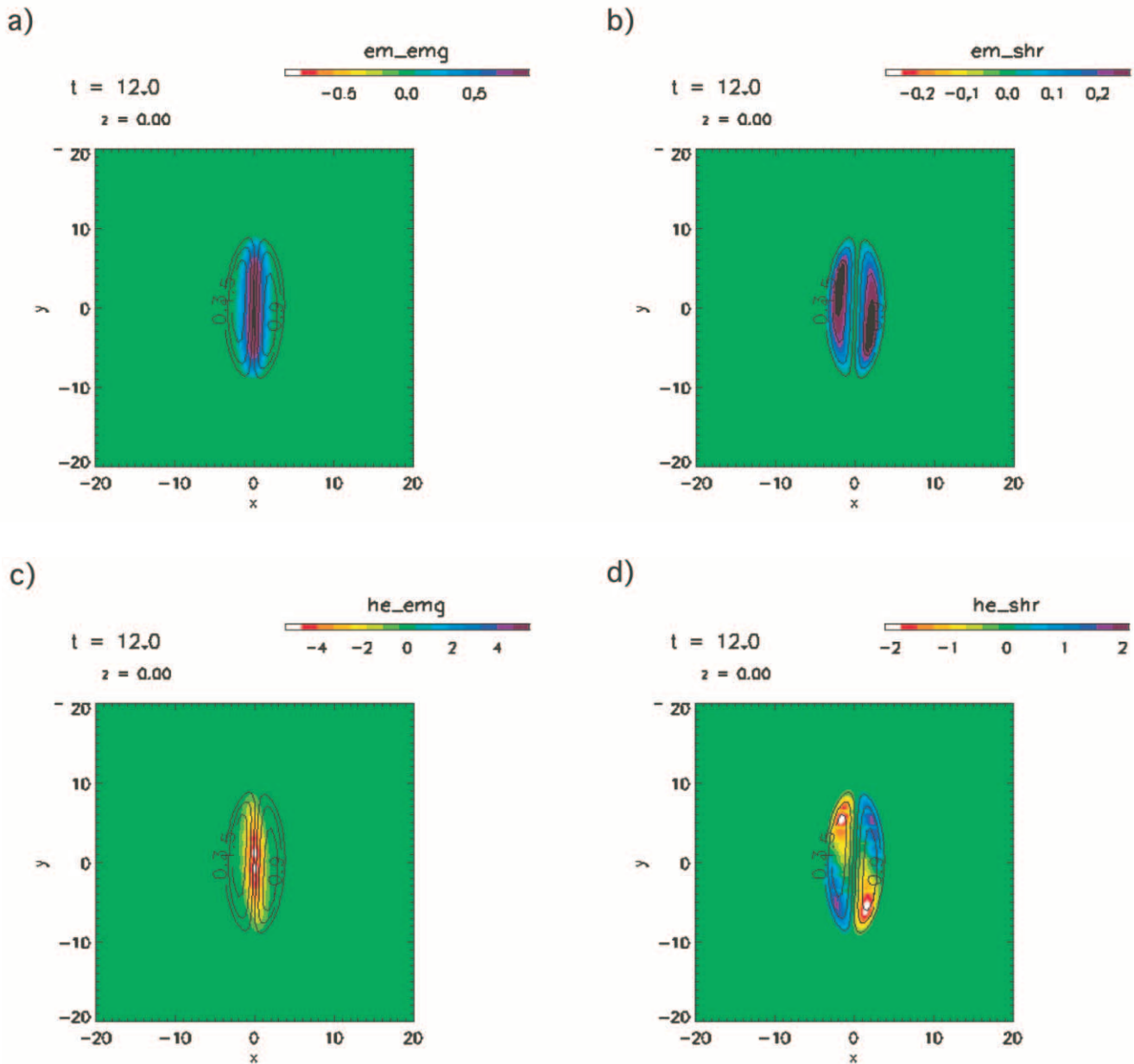


FIG. 10.—(a) Top-view snapshot taken at $t = 12$. A color map and contours on this map show the second term (emergence term) of eq. (22) and vertical magnetic flux, respectively. (b) Same as (a) but for a color map showing the first term (shear term) of eq. (22). (c) Same as (a) but for a color map showing the second term (emergence term) of eq. (23). (d) Same as (a) but for a color map showing the first term (shear term) of eq. (23). (e–h) Same as (a–d), respectively, but for $t = 36$.

magnetic forces, so it continues to pull the concave portion down to the photosphere and the field line finds some quasi-equilibrium state under the balance between the gravity and gas-pressure force. On the other hand, if the magnetic forces are strong enough to support the concave portion against the gravity, the concave portion gradually rises and eventually reaches the position where the magnetic pressure force plays a dominant role in expanding the whole field line.

In the field lines composing an emerging flux tube, the outer field lines are expanding field lines. Since they have a relatively strong poloidal component in the flux tube, the emerging outer field lines overlie the neutral line almost transversely. Emerging after the outer field lines are the inner field lines, initially distributed near the tube's axis. Compared to the outer field lines, the inner field lines appear

on the photosphere with a large footpoint separation, so they are undulating field lines. After they emerge, the inner field lines are almost aligned with the neutral line because they have a strong toroidal component in the flux tube. During the emergence, a simple diverging pattern of photospheric flow appears at the initial phase and later the flow shears across the neutral line, which is consistent with the observational result on emerging flux regions (Strous et al. 1996).

The simulation shows that the concave portion of the central field line, described in § 3.1 (originally corresponding to the axis of flux tube), sinks at first and later expands outward. Here it should be emphasized that the evolution to the final state of the central field line seems to be quite model dependent. Fan (2001) used a flux tube whose internal

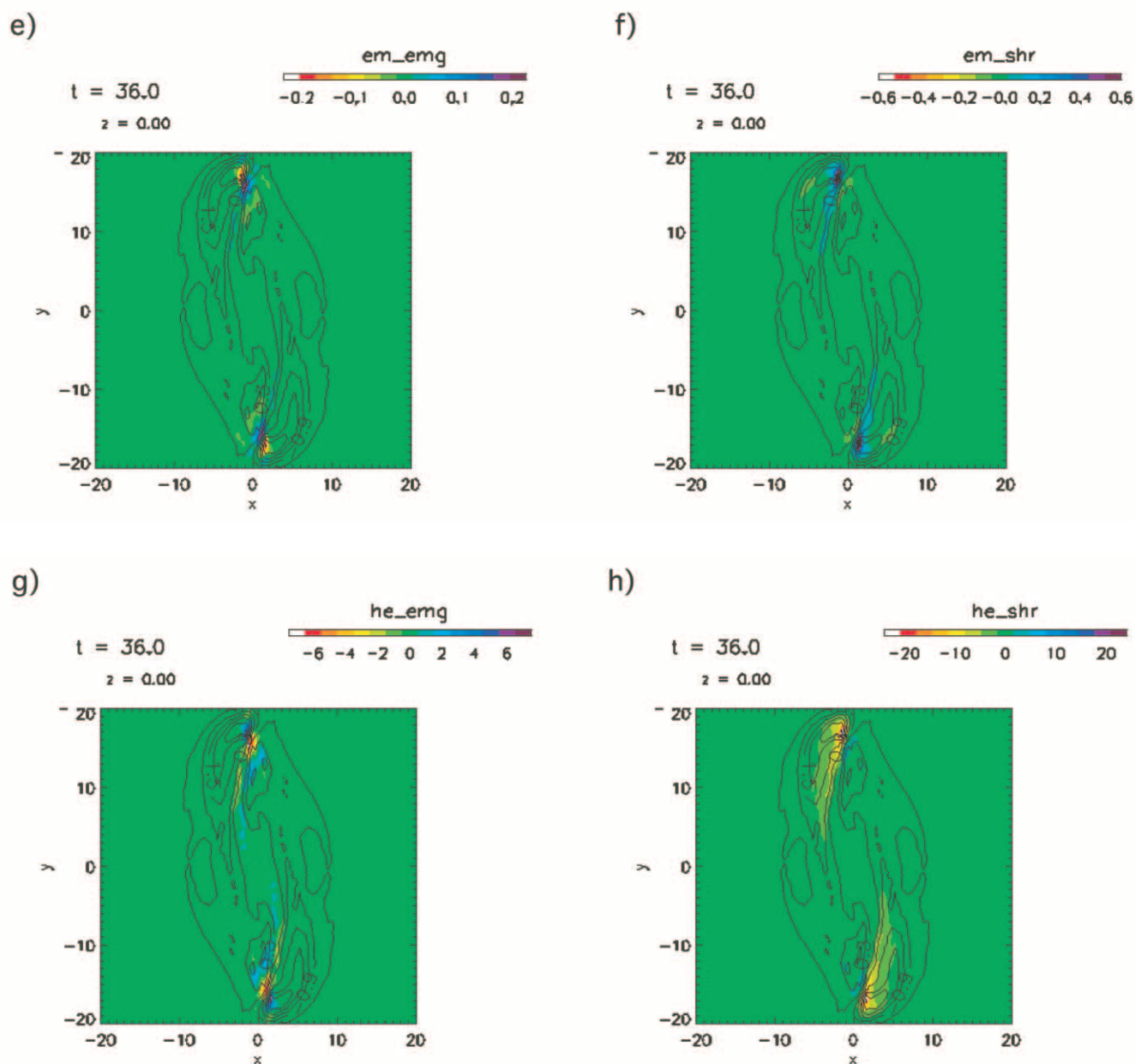


FIG. 10.—Continued

structure is different from ours and found that the central field line never expanded outward. In addition, it should be mentioned that the present simulation assumes an antisymmetry of the velocity field with respect to the z -axis, which prohibits unidirectional flows along emerging field lines such as siphon flow. It remains an open question as to how the central field line evolves to its final state in all possible types of emergence scenario. To answer this question it will be necessary to simulate a wider ranging class of magnetic flux tubes.

Arch filament systems are one of the observed phenomena whose shape and motion can be explained by the model presented. At the beginning of the emergence, an AFS observed in $H\alpha$ takes the form of dark loops connecting opposite-polarity regions across the neutral line. A plasma filling those loops moves upward in the middle of the loop and flows downward along its legs. These observed proper-

ties are reproduced by the simulation, in which the emergence starts with the appearance of the outer field lines of a flux tube, which overlie the neutral line at almost a right angle. The simulation also shows that there is an upflow in the middle of the emerging field line and a downflow along the field line. More detailed comparison between AFSs and the model of expanding field lines is found in Shibata et al. (1989, 1990) and Fan (2001).

As is already shown, the emergence of a twisted flux tube naturally forms the structure where the outer expanding field lines overlie the inner undulating field lines that are almost aligned with the neutral line. Focusing on this magnetic structure itself, there is a similar structure in helmet streamers, where a prominence lying along the neutral line is overlaid by an arcade-like structure expanding outward. The simulation also shows a transition of undulating field lines from an undulating state to an expanding state

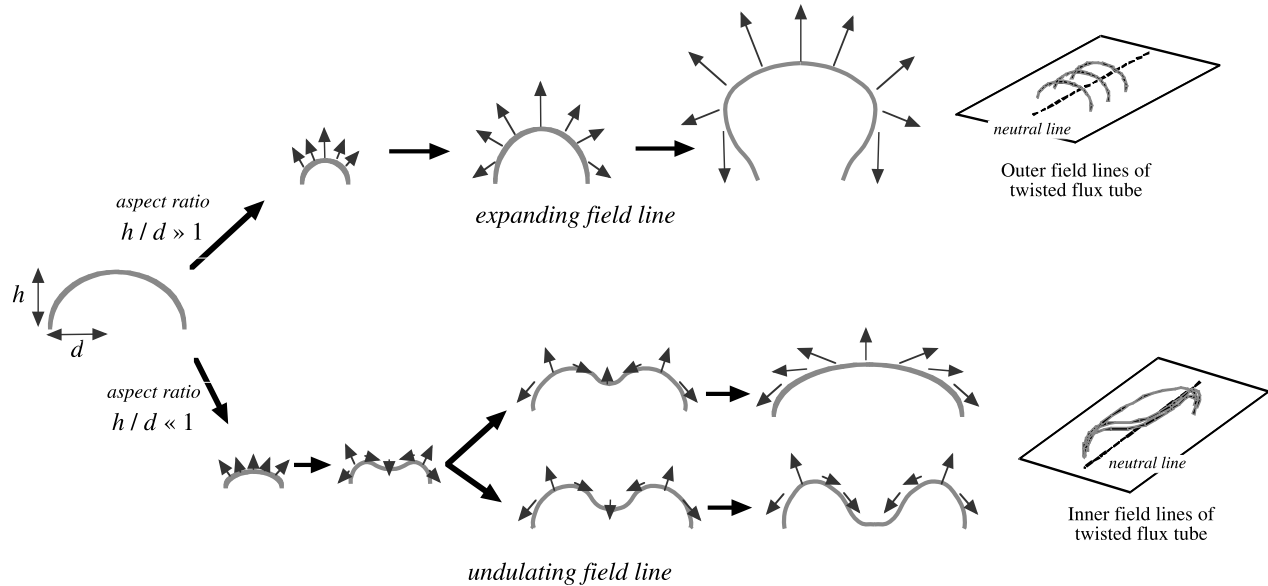


FIG. 11.—Schematic illustration of the evolution of emerging field lines that are classified into two groups, expanding field lines and undulating field lines. The expanding field lines keep a simple convex shape all through the evolution, while a dipped structure is formed in undulating field lines. The subsequent evolution of undulating field lines is either to expand outward or to sink toward the photosphere by developing the dip. A three-dimensional illustration of emerging field lines is presented at the right side of the figure.

(e.g., the central field line). If such a transition actually occurs in helmet streamers, then this might be one of the key factors initiating coronal mass ejections (CMEs), although the actual evolution is quite different from the adiabatic gas law assumed in our simulation. In order to clarify the role played by undulating field lines in CMEs, we should study their dynamical behavior under more realistic conditions where the processes of thermal conduction, radiative cooling, and heating are considered. In this respect, recent work by Antiochos, Macneice, & Spicer (2000) studies the dynamical nature of a plasma located on a U-shaped field line using the one-dimensional model that includes those diffusive processes. This work shows a cyclic dynamical behavior of a plasma that accumulates, moves, and drains from the field line.

There are also phenomena that could be modeled on the lower field lines described in § 3.1 whose concave portion is located below the photosphere. An example of such phenomena is the so-called U loops, which appear in the photosphere with their concave portion below the photosphere (Lites et al. 1996; Zwaan 1992). Emergence of U loops has been used as a conceptual idea to explain the “cancellation” of photospheric magnetic polarities (Low 1996), and recently the direct observation of an emerging U loop was reported by van Driel-Gesztelyi, Malherbe, & Démoulin (2000). According to the simulation, the subphotospheric concave portion of the lower field lines does not emerge into the photosphere completely, although that portion tends to approach the photosphere in an asymptotic way.

Sigmoids are also widely studied because they often appear as a precursor of eruptive phenomena such as CMEs (Rust & Kumar 1996; Canfield, Hudson, & Pevtsov 2000). Here we make a brief comment on the sigmoidal structure reported in our previous paper (Magara & Longcope 2001). That paper suggests that field lines with strong footpoint current are illuminated and observed as a sigmoid in soft X-rays. According to the present study, those field lines are

categorized as “expanded” undulating field lines, which are initially located just below the axis of a flux tube. Since high current density is distributed near the axis of the flux tube, strong current naturally flows along those expanded undulating field lines.

5. SUMMARY

This paper presents a detailed investigation of the dynamics of emerging magnetic field lines that originally compose a twisted flux tube. We find that emerging field lines are classified into two groups: expanding field lines that emerge with a large aspect ratio and undulating field lines that emerge with a small aspect ratio. The expanding field lines simply inflate into the outer atmosphere, while the undulating field lines remain in the lower atmosphere at least temporarily. In later evolution, undulating field lines either expand outward or sink to the photosphere, depending on the force balance at the concave portion of field line. More extensive studies of undulating field lines in three-dimensional geometry will undoubtedly prove to be very instructive for the understanding of solar phenomena, such as prominences and sigmoids.

We also study magnetic energy and helicity injection into the atmosphere as a result of flux emergence. This process is basically carried out by two kinds of motions at the base of the atmosphere, shearing motions and emerging motions. During the early phase of emergence, the emerging motions play a dominant role in injecting energy and helicity while the photospheric area of magnetic polarity regions is expanding. As the emergence becomes saturated, however, the polarity region deforms and fragments by shearing motions, and these motions become the main contributor of energy and helicity injection into the atmosphere.

T. M. deeply appreciates the discussion with the attendees of the ITP program “Solar Magnetism and Related

Astrophysics” held in Santa Barbara in 2002, which helped to develop this work. The numerical computations were carried out using the facilities of the National Institute of

Fusion Science in Japan and the National Center for Atmospheric Research in the US. This work is supported by AFOSR grant F49620-00-1-0128.

REFERENCES

- Abbett, W. P., Fisher, G. H., & Fan, Y. 2000, *ApJ*, 540, 548
 Antiochos, S. K., MacNeice, P. J., & Spicer, D. S. 2000, *ApJ*, 536, 494
 Berger, M. A., & Field, G. B. 1984, *J. Fluid Mech.*, 147, 133
 Böhm-Vitense, E. 1958, *Z. Astrophys.*, 46, 108
 Canfield, R. C., Hudson, H. S., & Pevtsov, A. A. 2000, *IEEE Trans. Plasma Sci.*, 28, 1786
 Choudhuri, A. R., & Gilman, P. A. 1987, *ApJ*, 316, 788
 DeVore, C. R. 2000, *ApJ*, 539, 944
 DeVore, C. R., & Antiochos, S. K. 2000, *ApJ*, 539, 954
 Dorch, S. B. F., Gudiksen, B. V., Abbett, W. P., & Nordlund, Å. 2001, *A&A*, 380, 734
 Dorch, S. B. F., & Nordlund, Å. 2001, *A&A*, 365, 562
 D’Silva, S., & Choudhuri, A. R. 1993, *A&A*, 272, 621
 Emonet, T., & Moreno-Insertis, F. 1998, *ApJ*, 492, 804
 Fan, Y. 2001, *ApJ*, 554, L111
 Fan, Y., Fisher, G. H., & McClymont, A. N. 1994, *ApJ*, 436, 907
 Finn, J. M., & Antonsen, T. M. 1985, *Comments Plasma Phys. Controlled Fusion*, 26, 111
 Fisher, G. H., Fan, Y., & Howard, R. F. 1995, *ApJ*, 438, 463
 Howard, R. F. 1991, *Sol. Phys.*, 136, 251
 Kusano, K., Maeshiro, T., Yokoyama, T., & Sakurai, T. 2002, *ApJ*, 577, 501
 Lites, B. W., Leka, K. D., Skumanich, A., Martinez Pillet, V., & Shimizu, T. 1996, *ApJ*, 460, 1019
 Longcope, D. W., Fisher, G. H., & Arendt, S. 1996, *ApJ*, 464, 999
 Low, B. C. 1996, *Sol. Phys.*, 167, 217
 Magara, T. 1998, Ph.D. thesis, Univ. Kyoto
 ———. 2001, *ApJ*, 549, 608
 Magara, T., & Longcope, D. W. 2001, *ApJ*, 559, L55
 Manchester, W. 2001, *ApJ*, 547, 503
 Matsumoto, R., Tajima, T., Chou, W., Okubo, A., & Shibata, K. 1998, *ApJ*, 493, L43
 Rust, D. M., & Kumar, A. 1996, *ApJ*, 464, L199
 Schüssler, M. 1979, *A&A*, 71, 79
 Shibata, K., Tajima, T., & Matsumoto, R. 1990, *Phys. Fluids B*, 2, 1989
 Shibata, K., Tajima, T., Steinolfson, R. S., & Matsumoto, R. 1989, *ApJ*, 345, 584
 Spruit, H. C. 1981, *A&A*, 98, 155
 Stein, R. F., & Nordlund, Å. 1998, *ApJ*, 499, 914
 Stix, M. 1991, *The Sun: An Introduction* (Berlin: Springer)
 Strous, L. H., Scharmer, G., Tarbell, T. D., Title, A. M., & Zwaan, C. 1996, *A&A*, 306, 947
 Tajima, T., & Shibata, K. 1997, *Plasma Astrophysics* (Reading: Addison-Wesley)
 van Driel-Gesztelyi, L., Malherbe, J.-M., & Démoulin, P. 2000, *A&A*, 364, 845
 Vernazza, J. E., Avrett, E. H., & Loeser, R. 1981, *ApJS*, 45, 635 (VAL)
 Zwaan, C. 1992, in *Sunspots: Theory and Observations*, ed. J. H. Thomas & N. O. Weiss (NATO ASI Ser. C, 375; Dordrecht: Kluwer), 75